Author Contributions:
Conceptualization: M. Jolivet, O. Dauteuil, L. Barrier
Data curation: M. Jolivet, A. Dia, M. Davranche, L. Barrier
Formal analysis: M. Jolivet, M. Davranche, A.-C. Pierson-Wickmann, L. Barrier, Nashaat Mazrui, R. Marsac, Xiangzhong Li

Highly Contrasted Geochemical Pattern in Sediments of the Okavango Delta, Botswana Driven by Dust Supply, Hydrological Heritage and Biogeochemical Reactions

M. Jolivet[1], O. Dauteuil[1], A. Dia[1], M. Davranche[1], A.-C. Pierson-Wickmann[1], L. Barrier[2], M. Murray-Hudson[3], Nashaat Mazrui[3], R. Marsac[1], Feng Cheng[4], and Xiangzhong Li[5]

[1]Géosciences Rennes—UMR CNRS6118, University Rennes, Rennes, France, [2]Laboratoire de Tectonique et Mécanique, IPGP, University of Paris, Paris, France, [3]Okavango Research Institute, University of Botswana, Maun, Botswana, [4]Key Laboratory of Orogenic Belts and Crustal Evolution, Ministry of Education, School of Earth and Space Sciences, Peking University, Beijing, China, [5]Key Laboratory of Earth System Science, Yunnan University, Kunming, China

Abstract The Okavango Delta in North Botswana is a hot-spot of biodiversity within the semi-arid central part of the South African plateau. This endorheic ecosystem is highly dependent on the annual flood that brings freshwater from the highlands of Angola to the North. However, in many places, the groundwater of the Delta is saline and contains very high concentrations of metal and metalloid elements, making it toxic to the flora and fauna. These saline waters have been largely studied and their formation is generally explained through evaporation and evapotranspiration processes. However, no studies have investigated the geochemical composition of the sediments that host the aquifers. Here, we provide a complete sedimentological and geochemical investigation (major, traces and rare earth elements, carbon and oxygen stable isotopes ratios, Sr and Nd isotope ratios) of the various geomorphological and ecological compartments that form the landscape of the SW Okavango Delta. We demonstrate that the non-connected underground aquifer is capped by a clay layer corresponding to a major event of dust deposition from the Makgadikgadi pan. We suggest that this aquifer may extend outside the island, below the floodplain and that the hydrological structure of the Nxaraga area is indeed composed of two non-connected aquifers of different origins. Challenging the model based on evaporation and evapotranspiration, we propose that the composition of that allochtonous clay and the in situ reactions between sediment, water and organic matter in a confined aquifer explain the geochemical enrichment of the water.

1. Introduction

The Okavango Delta in North Botswana is one of the few active alluvial mega-fans developing in an endorheic setting (Assine & Soares, 2004; McCarthy, 2013) (Figure 1). This fan forms a vast swamp flooded annually by water from the highlands of Angola to the North and it supports an exceptional ecosystem in the middle of the semi-arid Kalahari Desert. Due to their isolation, endorheic ecosystems result from tight coupling between climatic, topographic and geologic settings. Changes in one or several of these controlling factors have dramatic effects on the fragile equilibrium of the ecosystems, especially in semi-arid or arid climate contexts (Yapiyev et al., 2017). In the context of rapid climate change and of a regionally increasing anthropogenic pressure, especially on water resources (Ministry of Mineral, Energy and Water Affairs, Republic of Botswana, 1997), improving our knowledge of the structure and functioning of the sensitive Okavango geo-ecosystem is a fundamental challenge. Among the major threats to the ecosystem of the Delta, a decrease in the amount and quality of the water is probably the most important. In order to evaluate the impact of global change on the ecosystem, it is thus necessary to fully understand the hydrology of the Delta. In that respect, describing the geometry, sedimentological structure and geochemical pattern of the various aquifers is essential to understand the geochemical exchanges between the surface and groundwater, the soil and the biosphere.

Many studies have already addressed the sedimentation, the hydrology and the vegetation dynamics of the fan in terms of sediment input or water dynamics. A majority of these studies also deal with the effects of anthropogenic activity such as, water pumping, or those of tectonic activity along the faults bordering the rift (Ellery & McCarthy, 1994; Gieske, 1997; Gumbricht et al., 2004; McCarthy, Stanistreet, & Cairncross, 1991; Modisi et al., 2000; Mosley Bufford et al., 2012; Oromeng et al., 2021; Pastier et al., 2017; Ramatlapeng et al., 2021, 2023; Ramberg et al., 2006; Wilson & Dinçer, 1976). Because water supply is a major driving parameter of the ecosystem dynamics, a large number of studies focused on the water chemical composition and bio-geochemical reactions

both in the channels and soils (Akoko et al., 2013; Atekwana et al., 2016; Bauer-Gottwein et al., 2007; Dauteuil et al., 2021; Huntsman-Mapila et al., 2006; McCarthy, 2006; Mladenov et al., 2008; Ramberg & Wolski, 2008; Wolski et al., 2005). These studies revealed the occurrence of high pH—high conductivity groundwater inside islands on each side of the main Chiefs Island (Figure 1). These islands act as bio-geochemical reactors concentrating salt in a brine drop below their central part, which is thought to progressively sink at depth within the aquifer due to density contrast (Bauer et al., 2004, 2006; Ellery & McCarthy, 1994; Milzow et al., 2009; Ramberg & Wolski, 2008). However, Huntsman-Mapila et al. (2011) and Dauteuil et al. (2021) showed that groundwater sampled in the central part of Nxaraga Island in the SW Delta is strongly enriched in metals and metalloids such as U, V, As and rare earth elements (REE). Although the chemical interactions between the groundwater and the host sediment may involve key processes governing this enrichment, no investigation of the detailed geochemical composition of the island sediment is available except for a few studies looking at major elements (McCarthy & Ellery, 1994; McCarthy, McIver, & Verhagen, 1991; Ringrose et al., 2008). Could the geochemistry of the sediment explain the peculiar composition of the water? Is that water geochemically equilibrated with the host aquifer? Are the surface and groundwater aquifer connected?

To further document the near-surface sedimentological structure and geochemical composition of the Okavango Delta islands, we investigated the sediment stratigraphy and their geochemical compositions in various key areas in and around the Nxaraga Island (SW region of the Delta—Figure 1). Nxaraga Island and the surrounding floodplain have already been widely documented, especially in terms of surface and groundwater composition and dynamics (Bauer-Gottwein et al., 2007; Dauteuil et al., 2021; Gumbricht & McCarthy, 2003; McCarthy, 2013; Mladenov et al., 2005, 2008; Ramberg & Wolski, 2008; Wolski et al., 2005; Wolski & Savenije, 2006), but no study addressed the sedimentary architecture and sediment chemistry. We show that two distinct aquifers are superposed, corresponding to two geochemically different sediment layers. Inside the island, the limited variation of the water table level induces the formation of an incipient calcrete layer, highly enriched in metals, metalloids and more specifically in REE, in equilibrium with the host sediment. The geochemical composition of the groundwater implies an absence of exchange between the surface and groundwater aquifers, challenging the brine-drop model of the evolution of those islands. Finally, we show that air-borne dust (hereafter the term "dust" will designate clay and silt particles carried by the wind as a suspension load) deposits play a major role in the structure and geochemistry of the Delta.

2. Geological Setting

2.1. The Okavango Rift Zone and the Okavango Delta Alluvial Fan

Forming the southwestern termination of the East African Rift System, the Okavango Rift Zone develops in a c.a. 700 × 750 km depression including the Okavango graben, the Makgadikgadi Basin and the Zambezi Basin (Fairhead & Girdler, 1969; Kinabo et al., 2007; Pastier et al., 2017) (Figure 1). Most of the subsidence in the Okavango graben occurs along the southern set of faults (Thamalakane and Kunyere faults) where the sediment thickness can be up to 600 m (Bufford et al., 2012; Campbell et al., 2006; Modisi et al., 2000; Podgorski et al., 2013). During the Pliocene, the Okavango Rift Zone was occupied by the c.a. 150,000 km^2 Lake Deception, which progressively shrank during the Pleistocene until near complete evaporation at Present time (Burrough et al., 2009; Grove, 1969; Livingstone, 1857; Moore et al., 2012). Sedimentation in the Okavango alluvial fan initiated during the Late Pliocene—Early Pleistocene during the retreat of Lake Deception (McCarthy, 2013; Moore et al., 2012; Podgorski et al., 2013; Ringrose, 2022). The hydrodynamics of the Delta has been strongly influenced by Quaternary climate fluctuations as indicated by a major switch from large (120–150 m wide) meandering channels prevailing between about 7 and 4 ka ago to the modern narrow (<20 m wide) channels system (Tooth et al., 2021). The 7 to 4 ka humid period was following a noticeably dry period that affected southern Africa from about 15 to 9 ka (Telfer & Thomas, 2007).

The modern Delta is a c.a. 22,000 km^2 swamp including over 150,000 islands emerging from a flat alluvial plain. Each year this alluvial fan (McCarthy et al., 1993) is fed by 6–14 billion cubic meters of water from the Cubango and Cuito rivers flowing from Angola to the North and merging to form the Okavango River in the Panhandle region (Hughes et al., 2006; Mendelsohn & el Obeid, 2004; Wilk et al., 2006; Wilson & Dinçer, 1976; Wolski et al., 2006, 2012, 2014). Local rainfalls occur mainly during the low-flood season (November to March), with an annual average of 450 mm (Kenabatho et al., 2012; Wolski et al., 2012) although significant variations are observed following multi-decadal oscillations (Wolski et al., 2012). Water supply through both flooding and
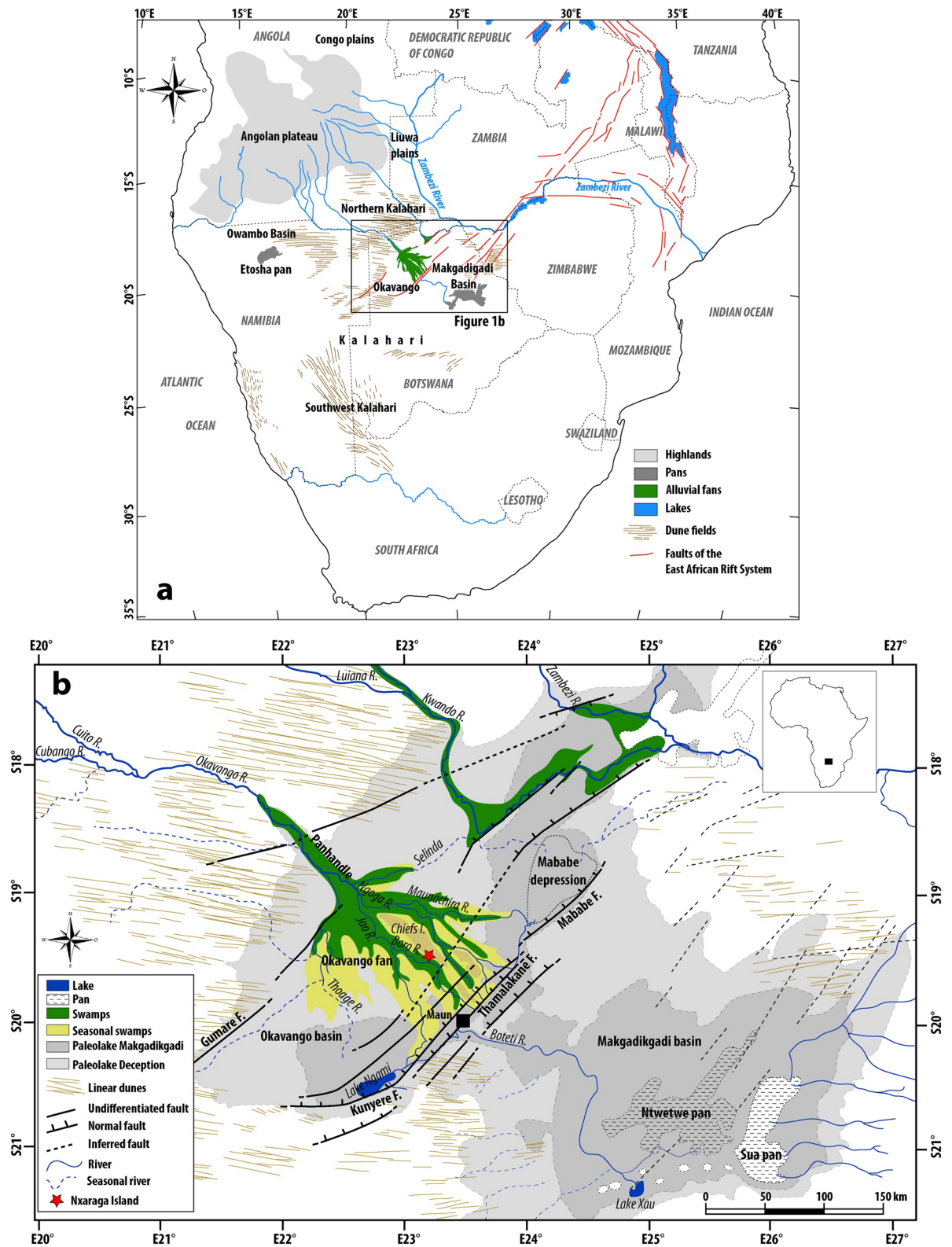
Figure 1.

rainfall is nearly balanced by evapotranspiration with only about 2% outflow through the Boteti River toward the Makgadikgadi Pan (Bauer et al., 2004, 2006) and limited internal storage although deep groundwater is present around, and possibly inside the Delta area (Milzow et al., 2009). An increasing amount of water is also used for human activities (Ministry of Mineral, Energy and Water Affairs, Republic of Botswana, 1997).

The fluvial sediments that progressively built the Okavango alluvial fan are mostly composed of the unconsolidated fine-grained aeolian sand deposits of the Kalahari Group eroded from the drainage system in Angola and Namibia (Garzanti et al., 2014; Haddon & McCarthy, 2005; Vainer et al., 2021). A significant proportion of dust material is also directly delivered or re-mobilized by wind into the Delta (Garstang et al., 1998; Humphries et al., 2014, 2020; Krah et al., 2004). The exogenous fraction of this fine-grained, nutrient-rich material mostly originates from the Makgadikgadi Basin (Humphries et al., 2020; Vickery & Eckardt, 2021). Geochemical analyses indicate that chemical weathering of the sediment source varies from minimal for the Aeolian sand fraction, to high in the material eroded from the highlands of Angola (Huntsman-Mapila et al., 2005). The clay fraction observed in the rivers is mainly formed by kaolinite (Humphries et al., 2020). In contrast, the non-organic component of the Aeolian dust (the dust being formed by erosion of the ground surface it also contains some varying amounts of organic matter (OM)) deposited on the surface is composed of smectite, with limited amount of kaolinite and illite (Garzanti et al., 2014; Ringrose et al., 2008).

The fan is characterized by several drainage subsystems (Wilson, 1973) (Figure 1). The water entering the fan from the Okavango River is distributed within three main channels: the Thaoge River to the West, the Jao and Boro rivers nearly axial to the fan, and the Nqoga and Selinda rivers to the East. However, most of the water is currently diverted eastward, whereas the Thaoge River to the West has been nearly inactive since a few decades. Northern and eastern regions of the Delta are characterized by heavily vegetated permanent swamps (Ellery et al., 1993; McCarthy et al., 1992; Tsheboeng, 2018; Tsheboeng et al., 2017). The southern part of the alluvial fan is active only during annual floods that peak in July and supports a semi-arid type vegetation of broad grasslands, shrubs and woodlands including several species of ficus, acacias and palm trees (Tsheboeng et al., 2017). Separating the Jao—Boro river system from the Nqoga one, the elongated Chiefs Island forms a dry land approximately 70-km-long and up to 12-km-wide, located within the axial part the fan (Figure 1).

2.2. Proposed Models for the Formation and Geochemical Evolution of the Okavango Islands

A large proportion of the Okavango islands displays a characteristic topography and vegetation pattern: the central part of the islands is generally flat, barren and surrounded by a ring of bushes and high grass. The outer part, immediately in contact with the floodplain, is formed by a 2- to 3-m-high ridge, supporting large trees such as, ficus, acacias, mopanes (*Colophospernum mopane*), lead-woods (*Combretum imberbe*) and palm trees (Figure 2).

Two main models have been put forward to explain the initiation and growth of the thousands of islands in the Okavango Delta. The first one involves zoogeomorphic processes (Whitesides & Butler, 2020) based on termite activity. Indeed, Macrotermes termites, widely represented in the region, build numerous mounds on the floodplain by accumulating and cementing fine-grained sediments. When the mound is large enough to emerge from the water during annual flooding, it can eventually be colonized by vegetation, forming a small proto-island (Dangerfield et al., 1998; McCarthy et al., 1998). However, this model is contradicted by the fact that Macrotermes termites cannot survive recurrent annual flooding lasting several months, preventing the initial development of the mounds on the floodplain (Davies et al., 2014; Muvengwi et al., 2016; Schuurman & Dangerfield, 1997).

The second model relies on topographic inversion of channels as a consequence of sediment dynamics. Many channels, especially North and East of Chiefs Island (Figure 1), are enclosed by aggrading peat banks formed by the strong accumulation of plant debris (mainly *Cyperus papyrus*) along the channel (Stanistreet et al., 1993). The growth of plants along and within the channel decreases the water-flow, lowers the bed-load sediment transport capacity and eventually raises the channel above the surrounding floodplain. The increased hydraulic gradient

Figure 1. (a) General map of southern Africa showing the main physiographic features. The East African Rift System is shown by the red fault-lines branch southwestward into the Okavango region (modified from Jolivet et al., 2022). Dune fields are from Thomas and Burrough (2012). (b) General map of the Okavango graben and Makgadikgadi Basin. The insert on the top right locates the study area. The Okavango Delta is located within the graben controlled by major faults belonging to the southwestern termination of the East African Rift system (e.g., Pastier et al., 2017). Dune fields are from Burrough et al. (2009) and Burrough and Thomas (2013). Prior to the deposition of this alluvial fan, the basin was filled by a series of extensive paleo-lakes such as Lake Deception and Lake Makgadikgadi (lakes extension areas are from Moore et al., 2012).
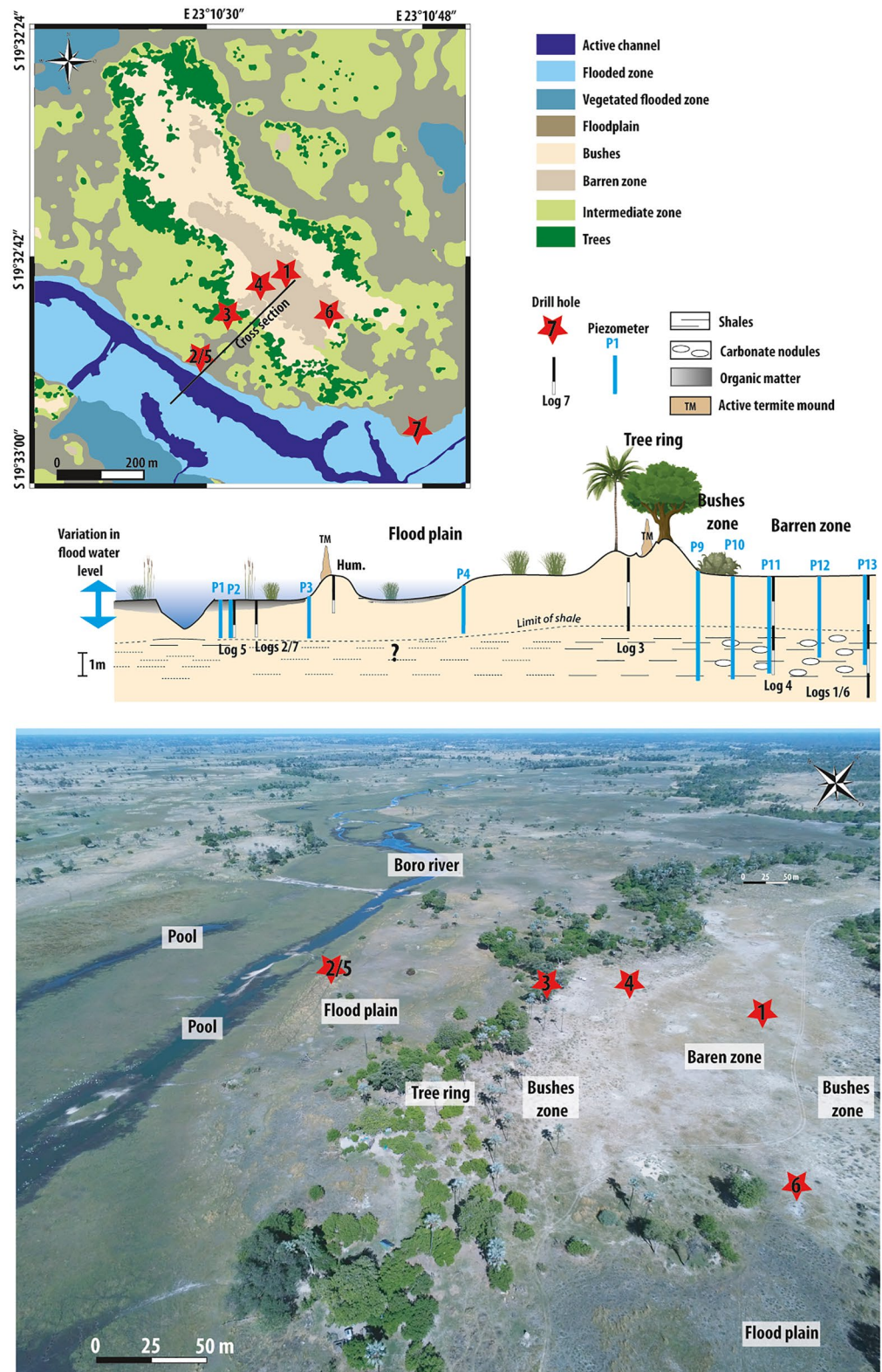
Figure 2. (top) Vegetation and geomorphic domains of Nxaraga Island and its surroundings with an indication of the location of the drill holes logged and sampled in this study; (middle) schematic cross section extending from the Boro channel to the central part of Nxaraga Island (see location map) and showing the position of the piezometers, as well as the projected position of the logs; (bottom), drone image showing the various geomorphological and ecological compartments around Nxaraga Island. The red stars indicate the position of the logs. Note that Log 7 is not on the image.

perpendicular to the channel leads to enhanced water seepage and eventually capture by a newly developed channel (Ellery et al., 1993; McCarthy et al., 1986, 1992). The peat eventually dries and is destroyed by fire, leaving the abandoned channels and their sandy deposits as positive reliefs forming islands (McCarthy, 2013). These are eventually colonized by vegetation (Ellery et al., 1993; McCarthy et al., 1986, 1992).

Following the initial colonization of the proto-island, the currently proposed model implies that plants play a major role in the island growth (Bauer et al., 2006; Bauer-Gottwein et al., 2007; McCarthy, McIver, & Verhagen, 1991; McCarthy et al., 1993). Water-consumption, especially from deep-rooted trees in the interior of the island leads to water circulation from the floodplain and from groundwater toward the island center. Due to evaporation and evapotranspiration, the water within the island progressively becomes enriched in salts, forming a dense brine drop (pH > 8) that sinks below the central part of the island (Bauer et al., 2004; Ellery & McCarthy, 1994; Milzow et al., 2009; Ramberg & Wolski, 2008). Salt precipitation kills the vegetation within the island, preserving only a ring of trees on the exterior where fresh water is available from the river and floodplain. Precipitation of calcite and silica increases the size of the island and the tree ring progressively migrates outward. Clastic material deposited by flooding or wind on the outer edge of the island and blocked by the vegetation (Humphries et al., 2020), participates to the lateral growth process whereas upward growth remains limited. This model requires a good hydraulic connectivity between surface water flowing in the channels and groundwater below the islands. However, based on water-table data, REE patterns and the concentrations of some metals and metalloids such as Pb, V, Cr, U, or As in ground- and river waters around Nxaraga Island, Dauteuil et al. (2021) questioned this model. Indeed, the REE pattern shape observed in the groundwater cannot be obtained from the concentration of the river water through evaporation or evapo-transpiration. The REE pattern observed in the river water was flat (normalized to Upper Continental Crust, UCC), whereas the REE pattern of the groundwater recovered in the central part of the island displayed a strong enrichment in heavy REE (Heavy Rare Earth Elements (HREE)) and strong positive Ce anomaly (see Figure 5 in Dauteuil et al., 2021). The authors suggested the occurrence of two disconnected aquifers, one corresponding to the surface flood and rainwater, and the second, at depth, corresponding to chemical-enriched water. The chemical enrichment in the second aquifer is explained either from leaching of dolomitic basement and/or from in situ biogeochemical processes. A similar disconnection between the river water—shallow groundwater of the Delta and the deep groundwater aquifers below and immediately around the Delta has also been demonstrated based on dissolved inorganic carbon (DIC analysis) (Akondi et al., 2019).

Obviously, deciphering between the various models presented above requires a better understanding of the geochemical composition of the sediments forming the islands and floodplains and of their interactions with the various aquifers. Below, we describe and discuss the stratigraphic structure and sediment geochemical composition of the various geomorphological compartments.

3. Materials and Methods

3.1. Nxaraga Island and Its Surrounding Floodplain

We focused our work on a well-studied, morphologically and ecologically representative island of the SW regions of the Delta. The 1000-m-long, up to 350-m-wide NW-SE elongated Nxagara Island is situated along the southwestern margin of Chiefs Island. It includes an outer ring of large trees and a central barren zone (Akoko et al., 2013; Bauer-Gottwein et al., 2007; Dauteuil et al., 2021; Gumbricht & McCarthy, 2003; McCarthy, 2013; Ramberg et al., 2006) (Figures 1 and 2). The latest is subdivided into two areas: one completely devoid of vegetation except for a few grasses and succulent plants, and a second covered with bushes, grasses, very few trees (generally dead) and some palm trees. The area covered with bushes dominates the northwestern part of the island with only a small barren surface along its eastern edge. By contrast, the barren zone dominates in the central and southeastern parts of the island where it forms an elongated depression connected to the floodplain. Satellite pictures analysis and field observations show that the barren zone is never flooded except for its southeastern-most part directly connected to the floodplain during the highest flooding episodes. Active termite mounds (*Macrotermes michaelseni*) are widespread in the area covered by the trees. Mounds still preserved in the bushes area have been abandoned and traces of long since abandoned ones, completely eroded, are visible in the barren zone. The Boro River that represents the main drain in that region of the fan, forms an about 20- to 30-m-wide and 1- to 2-m-deep clearly defined, sinuous channel (McCarthy et al., 1997). The active channel is embedded in an about 100- to 500-m-wide depression, annually flooded. A few large pools occur along the tributary channels, some of which are most probably reworked by animals (especially hippopotamuses) (Figure 2).

The alluvial plains around Nxaraga and the nearby islands are characterized by two topographic levels (Figure 2): the first level is formed by a floodplain incised by the river network (including the active channels and the major riverbeds), largely inundated during high flows, and covered with dense grass. A large number of hummocks, 1- to 2-m-high and 10- to 20-m-wide in diameter, some of them supporting bushes and palm trees, are distributed on the floodplain. Active termite mounds grow on some of the hummocks that support trees. However, no active termite mound has been observed on the floodplain itself both because no tree grows on these regularly flooded areas (Schuurman, 2006) and because the termite colonies cannot tolerate recurrent flooding (Davies et al., 2014; Muvengwi et al., 2016; Schuurman & Dangerfield, 1997). A second higher level of the floodplain is much drier, supporting not only grass but also small bushes, trees and palm trees. This intermediate surface is probably never or very seldom flooded, as assessed by the occurrence of active termite mounds.

3.2. Sediment Core Logging and Sampling

Sediment coring down to a maximum of about 5 m was conducted using manual drilling with a 15-cm-wide auger. A total of 7 sediment cores were drilled and logged on and around Nxaraga Island (Figure 2) in November 2018 (logs 1, 2, 3, 4, and 5) and July 2019 (logs 6 and 7). The November 2018 drilling campaign was performed after the receding of the annual flood and before the onset of the rain season. As year 2019 was exceptionally dry, the annual flood had not yet reached Nxaraga island in July, allowing both drilling campaigns to be performed in a dry period. The geographic coordinates of each log are available in Table S1. Log 4 Log 4 (4.2-m-deep) is located within the shrub-covered area, at the limit with the central barren zone of the island. Log 1 (5.5 m deep) is positioned in the middle of the non-flooded barren zone of the island. Finally, Log 6 (3.5-m deep) is situated in the eastern reach of the barren zone, inundated during the highest floods such as in 2020. Log 3 (3-m deep) is located within the tree ring on the southwestern side of the island. Logs 2, 5 and 7 were drilled in the floodplain. Logs 2 (0.9-m-deep) and 5 (1.5-m-deep) are located in the same area immediately near the Boro River. The drilling depth was limited by the occurrence of water near the surface that did not allow sediment recovery. Log 7 (1.4-m-deep) was drilled in July 2019 during a very dry season, SE of Nxaraga Island in the usually flooded depression enclosing the active Boro channel. For all these logs, a standard sedimentological analysis was performed to document the type of clastic material, the grain-size, the OM content and the occurrence of diagenetic features (such as carbonate nodules or oxides). Sediment samples were collected at 20–40 cm depth-intervals from 5 representative drill holes (logs 1, 3, 4, 5 and 6) in order to perform chemical analyses.

3.3. Sediment Granulometry and Mineralogy

Grain-size distribution was measured for each sample using a CILAS 1180 laser granulometer at LAGO Platform, CReAAH-Archeosciences laboratory, Observatoire des Sciences de l'Univers de Rennes (France). After decarbonation using HCl and destruction of the OM using H_2O_2, a few grams of sample were mixed with a solution of hexametaphosphate ($Na_6(PO_3)_6$) in an ultrasonic tank for 10 min to ensure grain separation before analysis. Measurements were repeated 3 times for each sample to ensure reproducibility.

Mineralogical analysis has been done on 6 key samples in order to evaluate potential links between the petrographic composition (especially the heavy minerals composition) and the bulk chemical composition. Samples were selected from three different depths in Log 1 (90, 350, and 415 cm depth) in the center of the island, two from Log 4 (113 and 345 cm depth) in the bushes area, and one from Log 5 (95 cm depth) in the floodplain. Sampling one drill hole in each geomorphic compartment allows to cover potential lateral composition variations from the floodplain to the central part of the island. In logs 1 and 4, the depth of the samples was selected so that potential depth-related variations will be covered. The respective proportions of quartz, feldspars and lithic clasts were determined on thin sections by counting at least 300 points using the Gazzi-Dickinson counting method (Ingersoll et al., 1984). After sieving between 50 and 250 μm, heavy minerals were separated through standard heavy liquid procedures before being mounted on a glass slide. 200 transparent heavy mineral crystals were point counted under a microscope except for sample L4-345 where only 95 crystals could be determined due to the small initial number of heavy minerals.

3.4. Water Sampling

Water samples were collected from piezometers within the Nxaraga Island and directly from the Boro River or adjacent channels during two field campaigns in October 2018 and July 2019. The year 2019 was a low flood year, the floodwater did not reach the Nxaraga Island and the Boro channel was partially dry. However, water

was present in the piezometers, including those inside the island. Piezometers were pumped dry or nearly dry and left to re-equilibrate during one night, reaching the near-same water level before sampling. A complete set of geochemical data on these water samples was recently published (Dauteuil et al., 2021) and we only report here newly acquired C and O stable isotope results.

3.5. Major and Trace Element Analysis

All the geochemical data obtained in this study are available in the Table S1, Tables S2 and S3 in Supporting Information S1.

3.5.1. Major and Trace Elements Analysis of Sediments

Bulk sediment samples were crushed to powder before analysis. Major and trace elements were measured at the central CNRS Service d'Analyses des Roches et Minéraux (so-called SARM) Center in Nancy (France) using an ICP-OES iCap6500 ThermoFischer for major elements and Sc, and an ICP-MS iCapQ ThermoFisher for trace elements. Data are available in Table S1.

3.5.2. Sr and Nd Isotope Analysis

Strontium and Nd isotopic analyses were measured at Géosciences Rennes using a 7 collectors Finnigan MAT 262 mass spectrometer. Samples were spiked with a ^{149}Sm-^{150}Nd and ^{84}Sr mixed solution and dissolved in a HF-HNO$_3$ mixture. Following dissolution samples were dried and taken up using concentrated HCl. NBS-987 Sr and Ames Nd-1 international standards were analyzed together with the samples, providing average ratio values of 0.710242 ($\pm$10) and 0.51196067 ($\pm$5) respectively. All the analyses of the samples have been corrected to the long-term ^{143}Nd/^{144}Nd ratio of 0.511963 (Ames Nd-1) or normalized to the NBS-987 ^{87}Sr/^{86}Sr reference value of 0.710250. Mass fractionation was monitored and corrected using ^{146}Nd/^{144}Nd = 0.7219 and ^{88}/Sr/^{86}Sr = 8.3752. Blank analyses provided values of <20 pg for Sr and <20 pg for Nd and were considered as non-significant. Data are available in Table S2 in Supporting Information S1.

3.5.3. Carbon and Oxygen Stable Isotopes Analysis

Carbon stable isotopes of dissolved organic (DOC—$\delta^{13}C_{DOC}$) matter in water and OM in sediments (SOM—$\delta^{13}C_{SOM}$) have been measured in the PISTE platform at Observatoire des Sciences de l'Univers de Rennes (OSU Rennes) using an EA-IRMS (ThermoFischer Smart EA coupled with a Delta V IRMS). All samples were acidified using HCl in order to remove any carbonate in sediments and waters. Both decarbonated sediments and dried waters were loaded into tin capsules. The $\delta^{13}C$ values are expressed as the relative deviation between the measured sample $^{13}C/^{12}C$ ratio and that of Vienna Pee Dee Belemnite (V-PDB) as follows: $\delta^{13}C$ (‰) = [(R$_{sample}$/R$_{standard}$) −1] × 1,000. No correction was added to the measured values, and the analytical uncertainty is estimated to be lower than 0.2‰. Oxygen and carbon isotopes were measured on carbonate nodules at the Qinghai Institute of Salt Lakes, Chinese Academy of Sciences, using a MAT253 with a GasBench II peripheral device. The results are expressed in delta (δ) notation relative to the V-PDB standard. The analytical errors of the laboratory standard were better than $\pm$0.1‰. Data are available in Table S3 in Supporting Information S1.

4. Results

4.1. Sedimentology and Stratigraphy of Nxaraga Island and the Boro Floodplain

The various logs obtained in this study are presented in Figure 3 and described from the center of the island to the channel. Grain-size measurements are shown in Figure 4. In the barren zone, Log 1 was obtained very close to an abandoned and completely leveled termite mound. The top of Log 1 down to 2 m is mainly composed of fine-grained white sand (>50%) and silt (20%–30%). The clay content remains low (~3 to 6%). No OM is visible (hereafter, the amount of OM is evaluated visually using the lighter or darker color of the sand relative to this white sand). Although efflorescent salt crusts have been reported on this island (Bauer-Gottwein et al., 2007), no salt was observed during fieldwork in November 2018 and July 2019, either on that island or on the nearby ones. At 2 m, the amount of clay and silt increases sharply to about 10%–15% and 40%–60%, respectively. Small black nodules interpreted as oxides are visible. By 2.4 m carbonate (reacting to HCl acid) nodules, about 0.5–1 cm in diameter are ubiquitous sediments, as well as mm-thin red oxidized organic-rich layers. The sediment becomes wet, indicating the top of the aquifer. Between 3- and 4.5-m-depth, the sediment is mainly composed of white, highly cohesive, clay-rich carbonated mud with cm-size clay nodules. Nodules are absent in the last meter.
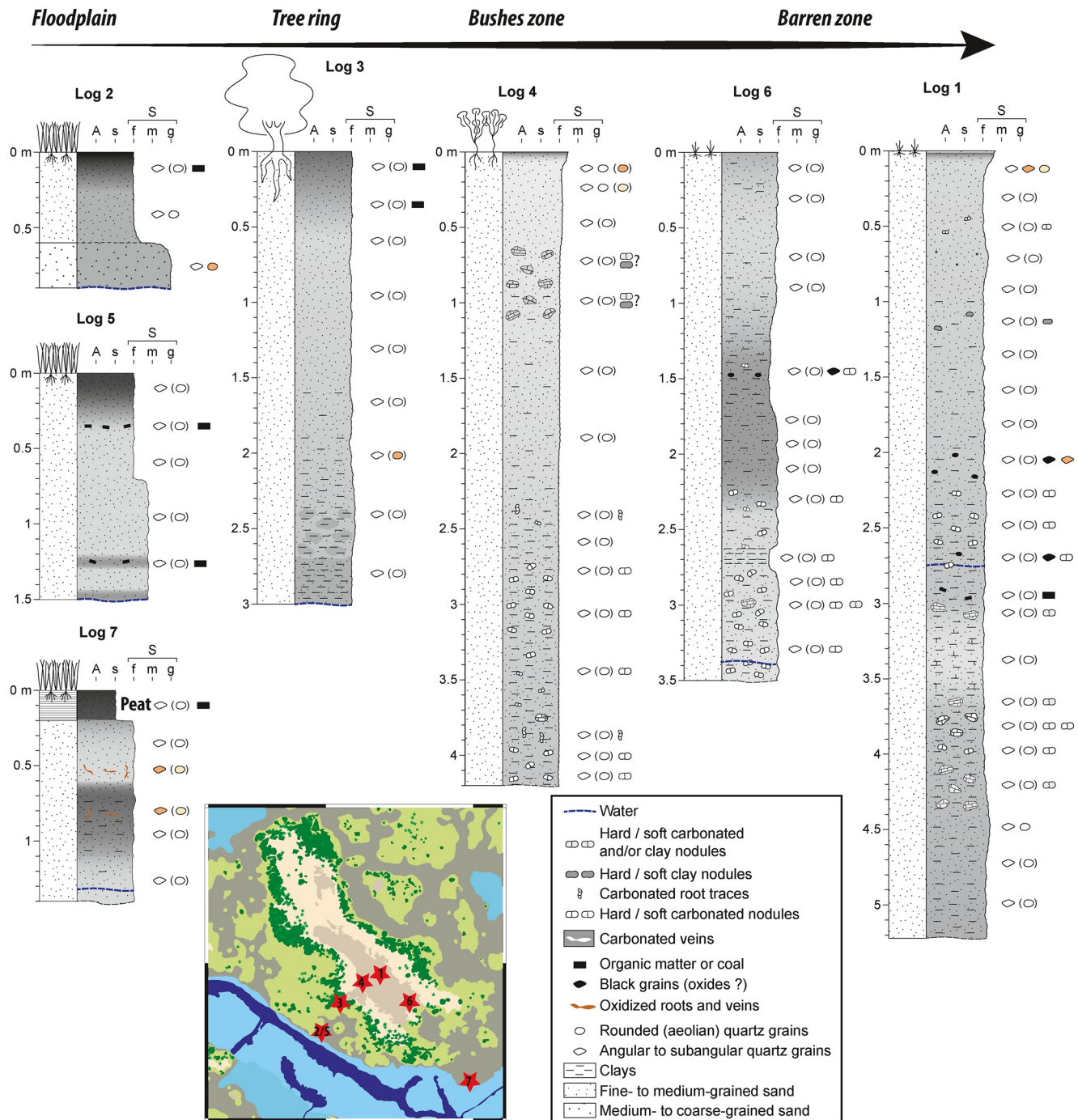
Figure 3. Sediment logs obtained from auger-drillings (see location on map). Darker colors indicate a higher organic matter content. The water level is indicated as on November 2018 (logs 1 to 5) and July 2019 (logs 6 to 8). See text for a detailed description.

The stratigraphy of Log 4 located close to the bushes area is similar to that of Log 1 except for the occurrence of a cemented sand layer containing 1–4 cm large clay-rich nodules between 0.6- and 1.2-m-depth. The amount of clay increases sharply to about 20%–30% below 3 m together with the occurrence of poorly hardened carbonate nodules, whose density increases downward. Water occurred at about 3-m-depth.

The top of Log 6 in the sometimes-inundated region of the barren zone is devoid of visible OM. The proportion of clay (14%) and silt (41%) is higher than in Log 1 but decreases sharply after a few centimeters before increasing again slowly. No salt is found on the surface. The first mm-size carbonate nodules are found around 1.2 m
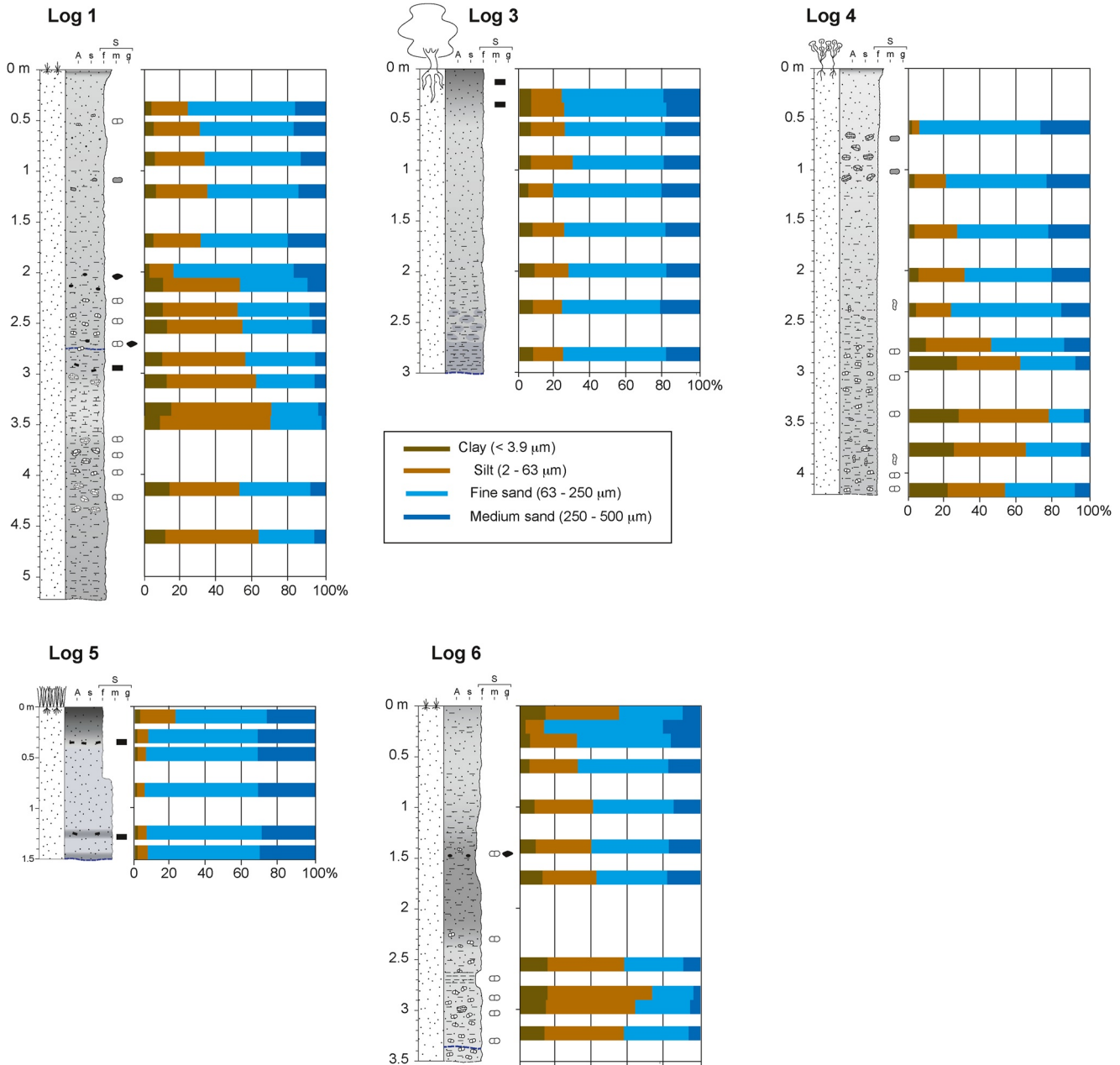
Figure 4. Sediment granulometry of all logs in Nxaraga island and floodplain. Grain sizes are divided into 4 groups ranging from clay to medium sand. No coarse-sand grains have been observed. The raw data graphs for all individual samples are available in the Graph 1 in Supporting Information S2 depository of the Open Science Framework (OSF) data repository attached to this work.

associated with an increase in OM and small black nodules. From 2.2 m, cm-size carbonate nodules are found in relatively white, clay-poor sand alternating with decimetric clay-rich, nodule-free layers. The density of nodules increases downward and the sand becomes humid at around 3.3 m.

The first 30 cm of Log 3, situated within the tree ring, are composed of fine- to medium-grained dark-gray sand (about 70%), silt (up to 17%), and a limited amount of clay (7%). The proportion of OM sharply decreases below 30 cm and the sand becomes white and well sorted. The proportion of clay slightly increases downward (up to 9%) but no carbonate nodule is observed. Water is found at about 3 m.

In the Boro floodplain, the first 20–30 cm of Logs 2 and 5 are composed of organic-rich fine- to medium-grained sand (up to ~75%) with a very low amount of clay (<2% except for a 3% value on the surface). Below 30 cm,

Table 1
Results of Petrographic Analysis of Selected Sediment Samples From the Three Vertical Compartments of the Nxaraga Island System

Samples	Q	F	Z	T	R	ZTR	Amp	Grt	Ep	AGE	Ap	Ky	Bt	Tot. h. (%)
Upper compartment														
L1-90	100	0	29.4	22.1	14.7	**66.2**	8.8	4.4	17.2	**30.4**	3.4			100
L4-113	98	2	18.5	19	8.5	**46**	39.5	0	5.5	**45**	9			100
L5-82	100	0	18.3	23.8	2	**44.1**	46	1.5	3.5	**51**	4.9			100
Middle compartment														
L1-350	99.8	0.2	10.5	22.4	5.2	**38.1**	34.3	1.4	22.4	**58.1**	2.9	0.9		100
L4-345	99.5	0.5	20	20	9.5	**49.5**	23.2	0	10.5	**33.7**	13.6	2.1	1.1	100
Lower compartment														
L1-415	100	0.2	15.5	14	13.5	**43**	31.5	5.5	17	**54**	3			100

Note. Q: quartz; F: feldspath; Z: zircon; T: tourmaline; R: rutile; Amp: amphibole; Grt: garnet; Ep: epidote; Ap: apatite; Ky: kyanite; Bt: biotite; ZTR (zircon + tourmaline + rutile); AGE (amphibole + garnet + epidote). The bold values are specific indexes (ZTR: zircon + tourmaline + rutile) and AGE (amphibole + garnet + epidote).

the sediment shows decimeter-thick white sand layers alternating with organic-rich sandy layers. Water is found at 0.9 m in Log 2 (drilled in November 2018) and at 1.5 m in Log 5 (drilled in July 2019 during an anomalously dry period). The amounts of silt (generally <6%) and clay (<2%) are low, and no carbonate nodule is observed. Finally, Log 7 shows peat on the first 20 cm from the surface. Below the sediment is composed of well-sorted sand with, from a visual inspection, a limited amount of OM. Water is present from 50 cm-depth. Below 60 cm, the amount of OM increases before decreasing from 1.1 m.

In summary, the sediments in both the island and floodplain are mainly composed of fine- to medium-grained, well-sorted sand with a variable amount of clay, silt and OM. The central part of the island is characterized by some carbonate precipitation associated to a sharp increase in clay and silt content at about 2–3 m depth corresponding to the groundwater table. No salt is observed on the surface as previously described. The floodplain is characterized by a lower amount of clay and silt, a 20- to 30-cm-thick organic rich layer on the surface with a relatively high amount of OM down to about 1 m.

4.2. Petrography

The petrographic analysis of the selected samples reveals that all compartments are composed of pure quartzose sand with >99% quartz and no lithic fragments (the clay fraction is not analyzed) (Garzanti, 2019) (Table 1 and Figure 5). Only sample L4-113 shows a slightly higher percentage (2%) of feldspars (mostly K-feldspars). The amount of heavy minerals separated from each sample does not vary significantly except for sample L4-345, which shows fewer crystals. Although the available samples were relatively too small to perform a state-of-the-art heavy minerals petrographic analysis, they are mostly represented by zircon, tourmaline, rutile, amphibole and epidote, with varying proportions of garnet and apatite and few crystals of biotite and kyanite. The ZTR index (zircon + tourmaline + rutile), that reflects the amount of recycling, is generally between 40 and 50, with two outliers at 66 (sample L1-90) and 38 (sample L1-350). The number of samples is limited, but there is no apparent relation between depth and ZTR values or between the logs and ZTR. Similar results were previously obtained by Garzanti et al. (2014) and Garzanti et al. (2022) on the Present-day Okavango system (including the Boro channel). The authors concluded that the sand from the Okavango system was essentially recycled from the Kalahari Group deposits, including large proportions of aeolian sand.

4.3. Major and Trace Elements Composition of Sediments

Major and trace element data are illustrated in Figure 6. The complete data set can be found in Table S1. The results are presented from the channel (Log 5) to the center of the island (Log 1).

In the alluvial plain, the major element chemistry of Log 5 is dominated by SiO_2 concentration, whereas other elements display concentrations of less than 1% (Figure 6a). A small increase in Al_2O_3 concentration (up to 1%) is observed around 0.5 m. The LOI (Loss On Ignition) indicator has to be related to sample decarbonation and/or dehydration of
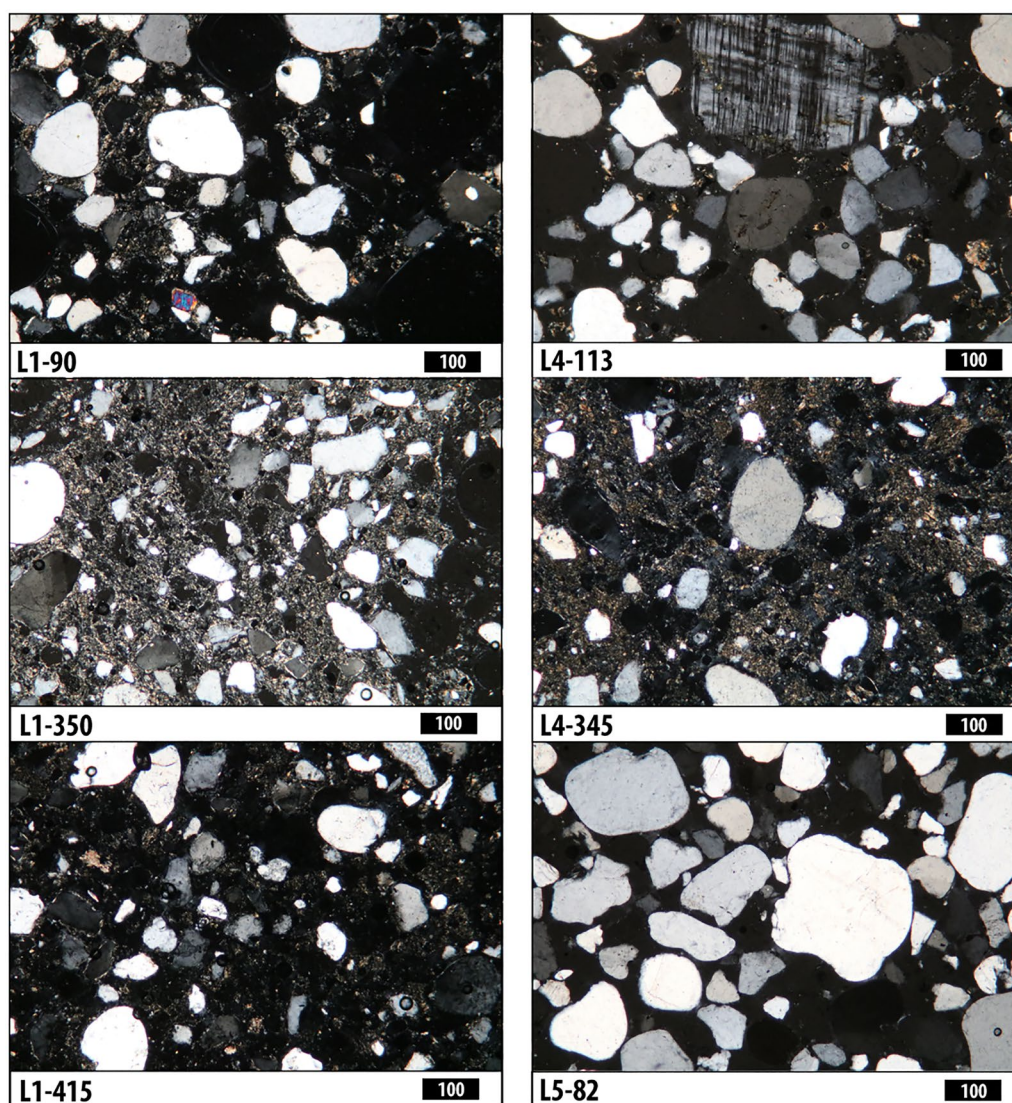
Figure 5. Microscope images of selected samples from the sediment of Nxaraga island (see text for discussion of the images). Most of the grains are quartz (all shades of white to black), the bright-colored mineral in sample L1-90 is an amphibole, while the large gray striated crystal in sample L4-113 is a K-feldpar. The "matrix" with bright colors is mostly composed of clay. As the initial samples are unconsolidated, this is not to be considered as a real matrix. All images were taken with crossed polars. The black bar marked 100 represents 100 μm.

clay layers. Trace element concentrations remain relatively constant along the log except for Cr, Rb, and Co that notably decrease close to the surface in an organic-rich layer. Log 3 is 3-m-deep, on the outer edge of the tree ring. SiO_2 again dominates the major elements chemistry; however, its concentration decreases by about 10% from about 1.5 m as those of Al_2O_3 and Fe_2O_3 start to increase (Figure 6a). CaO concentrations are below the detection limits. A similar pattern is observed for the trace element concentrations, with a noticeable increase (>x2) with depth for several elements including alkalines (Rb as an example), earth alkalines (such as Ba) and metals such as Co, Cr, and Pb.

Inside the island, Log 4 is located at the limit between the bushes zone and the central barren zone. The geochemistry of the sediments shows two marked compartments, above and below about 2.5 m from the surface (Figure 6b). Above 2.5 m, the major and trace element concentrations are similar to those observed in Log 3. Below 2.5 m the amount of SiO_2 decreases whereas nearly all the other element concentrations increase. This increase is coeval with the occurrence of both carbonate nodules and higher clay content (Figure 4) associated to an increase in Al_2O_3, Fe_2O_3, and LOI. Trace elements such as Cr (42 ppm around 3.5 m), Rb (45.6 ppm around 3.5 m), Zn, U, Zr, or V show high concentrations with Ba and Sr reaching peaks at 2,586 ppm around 3 m and 1,048 ppm around 4 m, respectively. In
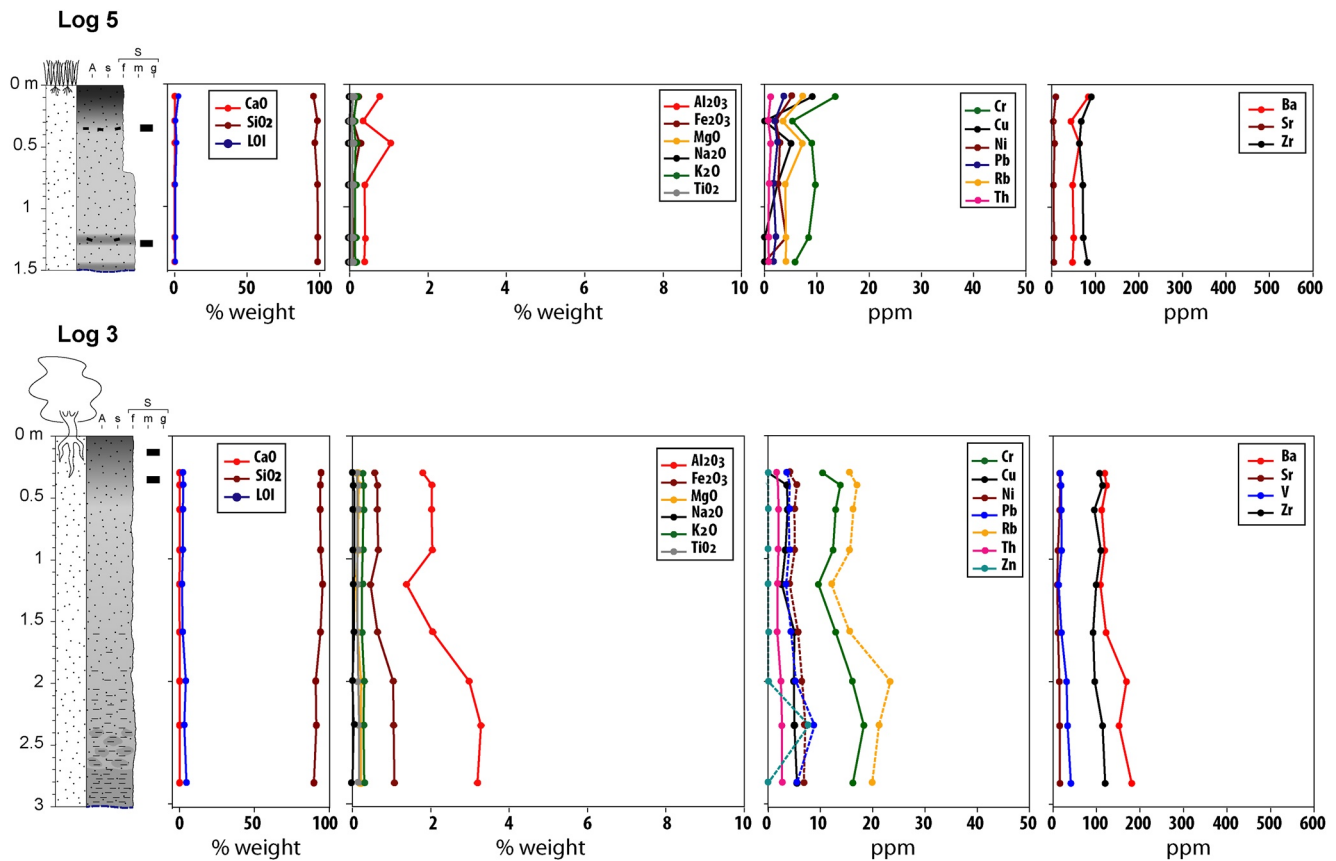
Figure 6. (a) Concentration versus depth of major, some selected trace elements and loss on ignition (LOI) values within the sediments of logs 5 (floodplain) and 3 (tree ring). Note that Ba and Sr concentrations have been cut at 600 ppm to allow a better reading of the figure. Concentration values measured elements, including those not shown in the figure, can be found in Table S1. See Figure 2 for the position of the logs. (b) Concentration versus depth of major, some selected trace elements and loss on ignition (LOI) values within the sediments of logs 4 (bushes zone), 1 (central barren zone) and 6 (external part of the barren zone). Note that Ba and Sr concentrations have been cut at 600 ppm to allow a better reading of the figure. Concentration values measured elements, including those not shown in the figure, can be found in Table S1. See Figure 2 for the position of the logs.

the center of the barren zone, Log 1 shows similar concentration patterns although the limit between both compartments is located between 1.5 and 2 m below the surface. Since the altitude of the surface of Log 1 is below that of Log 4 by about 1 m, the absolute depth of the limit between the two geochemical compartments is similar. K_2O and Na_2O concentrations remain below 2% and are nearly null within the first 2 m, advocating against the presence of salt on the surface. Metals such as Ni, Cu, Pb, Zn, Cr, or alkaline (Rb) again show high concentrations in the lower compartment, with alkaline earth (Ba) reaching a peak at 976 ppm around 4 m, although remaining lower than in Log 1. All the concentration peaks are associated with layers enriched in carbonate nodules and clays. The concentration in all elements is less variable in Log 1 than in Log 4 suggesting less sediment heterogeneities, possibly due to bioturbation by the close-by abandoned termite mound. In the two lowest samples of Log 1, the concentration of all the elements but Si decreases sharply to values almost identical to those in the upper compartment. This pattern is correlated to the lack of carbonate nodules. Finally, Log 6 is located within an occasionally flooded part of the barren zone (Figure 2). The geochemical pattern describes two compartments, with a limit around 1.5–2 m below the surface, an absolute position similar to that of the limit in logs 4 and 1 (Figure 4). K_2O and Na_2O are nearly null on the surface, indicating an absence of salt crust. Note that the flood was very low during that summer and the area around Log 6 had not been covered by water since several years (personal communication of ORI staff).

4.4. Rare Earth Element Distribution

The REE concentrations were normalized to the UCC following Taylor and McLennan (1985). The two geochemical compartments described above are again evidenced by markedly different REE patterns (Figure 7, Figure S1 in Supporting Information S1 and Table S1).
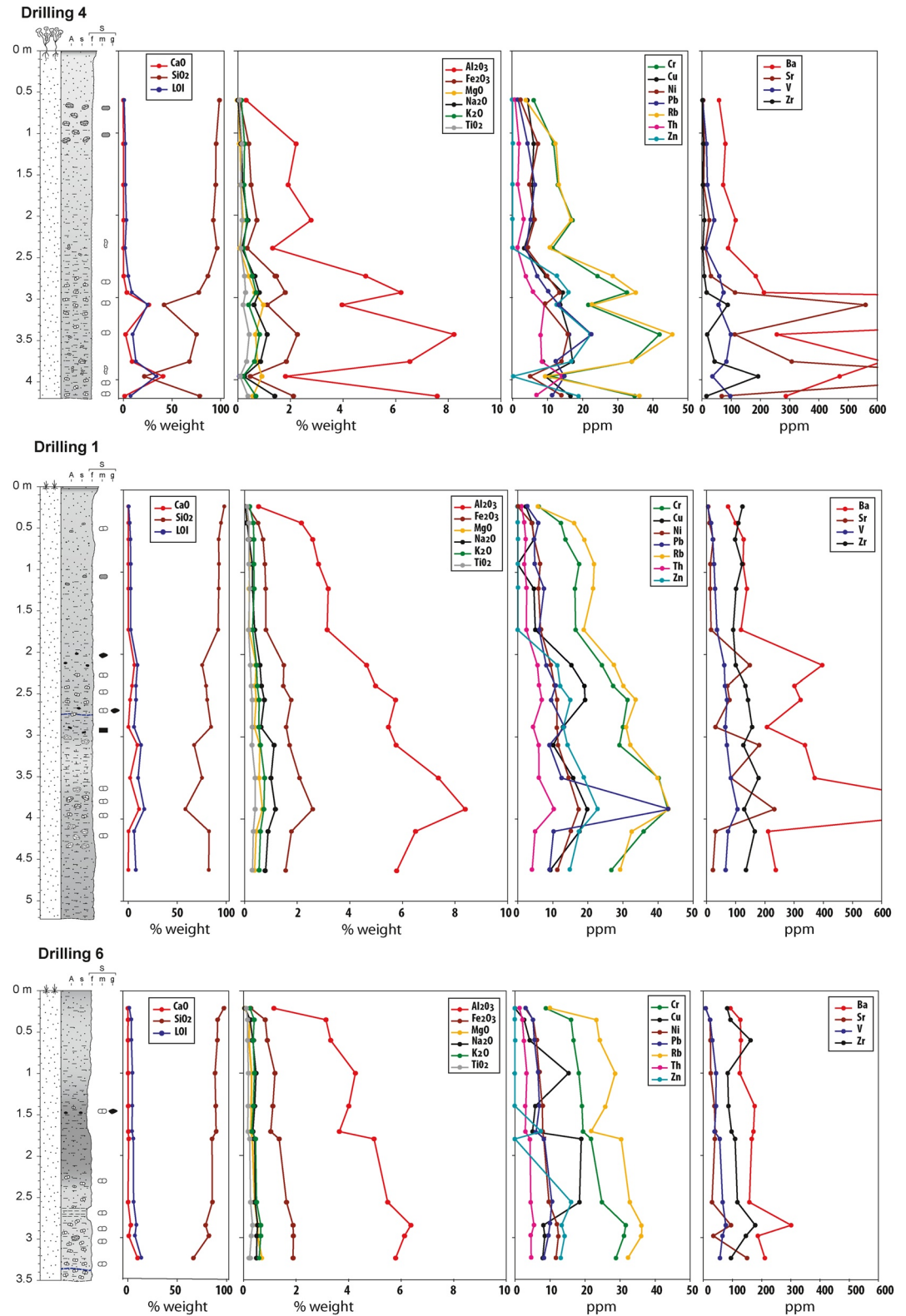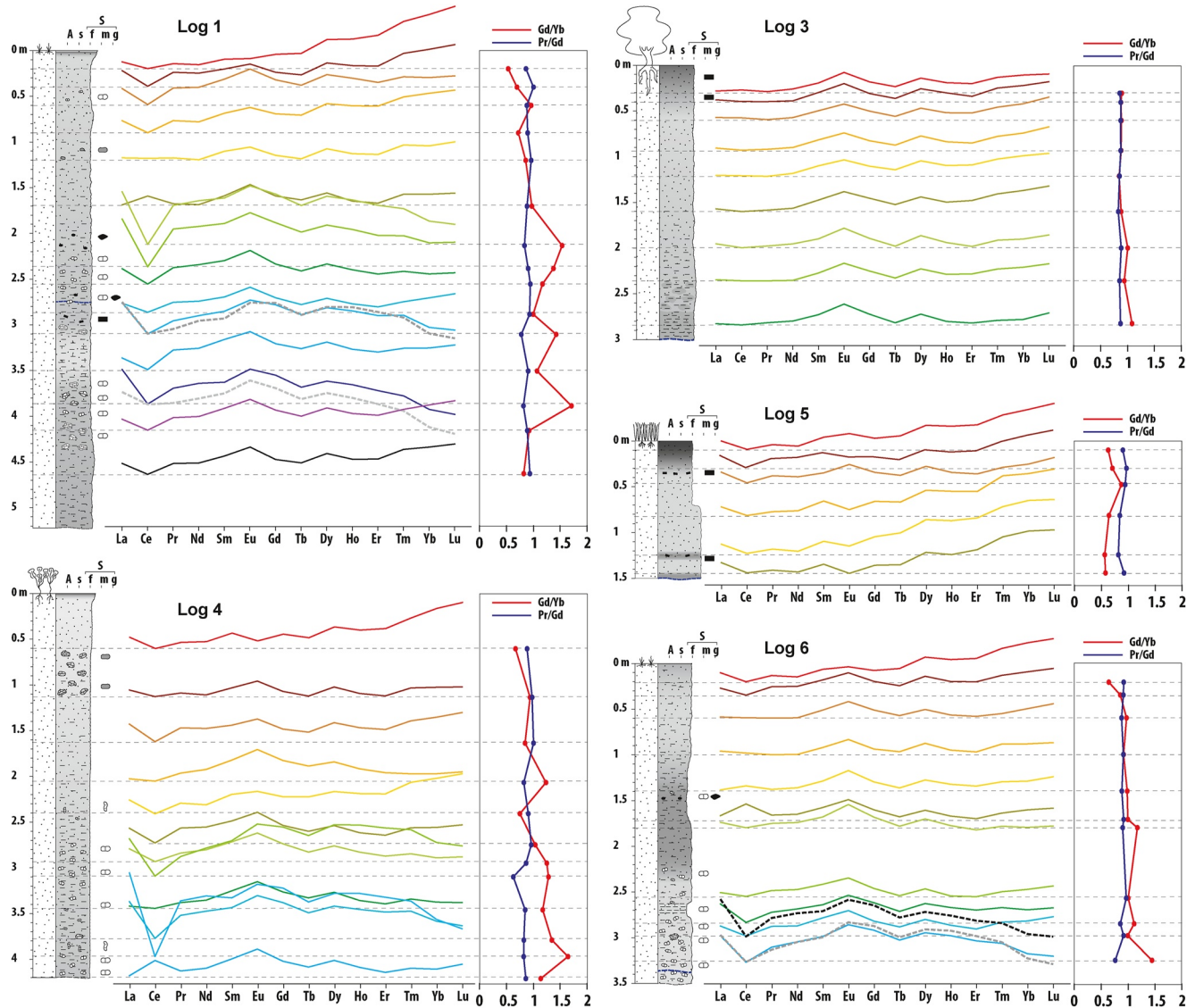
Figure 6. (Continued)

Figure 7. Rare earth elements (REE) versus UCC standard patterns versus depth in Logs 1, 3, 4, 5, and 6. The dotted lines indicate the position of each sample. See Table S1 for the REE concentration values in all the logs and Figure S1 in Supporting Information S1 for the sample versus UCC concentration ratios. For each log, the Gd/Yb and Pr/Gd ratios are indicated.

In Log 5 (close to the Boro channel), REE concentrations are low, with total REE concentrations (ΣREE) varying between 8.8 and 15 ppm (Table S1). The REE patterns are quite similar for all samples, with a marked enrichment in HREE (with $0.57 < Gd/Yb < 0.89$, Figure 7) and a small negative Ce anomaly ($0.85 < Ce/Ce^* < 0.91$) (Figure S2 in Supporting Information S1). In Log 3 (outer edge of the tree-ring), the concentrations are low but higher than those occurring in Log 5 and increase with depth (ΣREE = 25 ppm at the surface against 47 ppm at 1.4-m-depth). The REE pattern shapes are identical among them but differ from those of Log 5 by the absence of negative Ce anomaly, a slight HREE enrichment ($0.85 < Gd/Yb < 0.88$) and a positive Eu anomaly ($1.11 < Eu/Eu^* < 1.18$) (Figure S2 in Supporting Information S1).

Inside the island, Logs 4, 1, and 6 in the bush zone, the center of the barren zone and the seldom-inundated zone, respectively, show an evolution of the REE patterns through depth. Concentrations also vary, reaching a maximum at around 4 m from the surface. The highest concentrations are found in the carbonate nodules with ΣREE varying between 303 and 1,161 ppm in Log 1 nodules (Table S1). At shallow depth, below 1 m from the surface, the REE patterns and the ΣREE differ from those obtained in Logs 5 and 3: they display a slight HREE depletion ($0.9 < Gd/Yb < 1.23$ for Log 4, $0.97 < Gd/Yb < 1.7$ for Log 1 until 4 m, and $0.98 < Gd/Yb < 1.17$ for Log 6

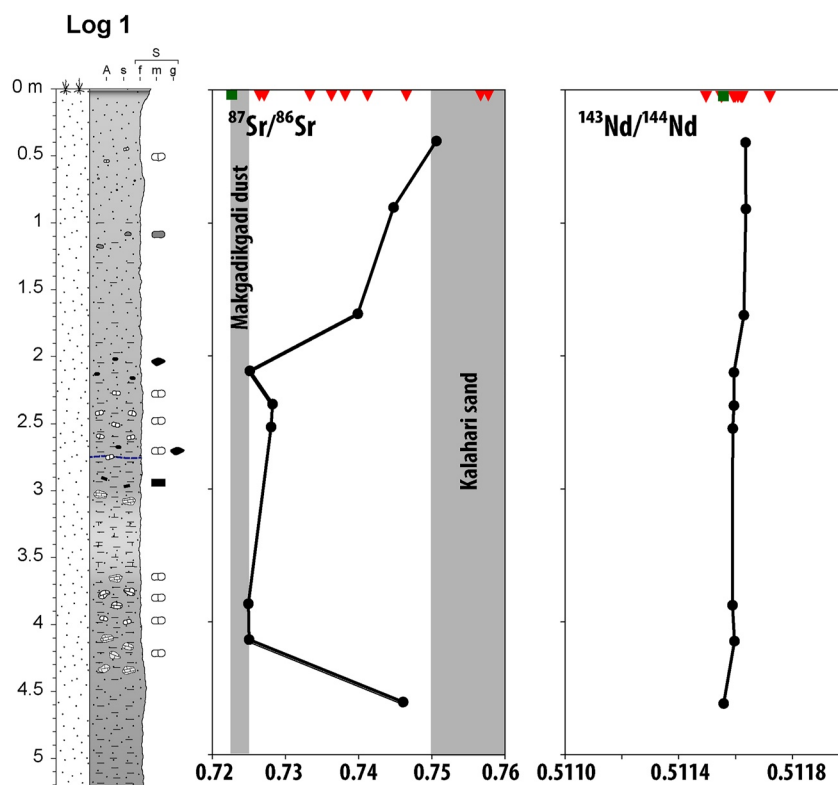**Figure 8.** $^{87}Sr/^{86}Sr$ and $^{143}Nd/^{144}Nd$ isotopic ratios obtained in Log 1 (black). The red triangles correspond to values obtained by Humphries et al. (2020) on island soils within the Okavango Delta and the green squares correspond to values obtained by Garzanti et al. (2014) on the mud fraction within the Boro channel).

(Figure 8)) and a small negative Ce anomaly (Figure S1 in Supporting Information S1). With depth, the initial HREE enrichment is replaced by HREE depletion while a positive Eu anomaly is developed, similar to Log 3 (1.14 < Eu/Eu* < 1.17, 1.10 < Eu/Eu*<1.20, and 1.15 < Eu/Eu* < 1.21 for Logs 4, 1, and 6, respectively) (Figure S2 in Supporting Information S1). Below 1 m, the negative Ce anomaly becomes more negative (0.68 < Ce/Ce* < 0.92, 0.48 < Ce/Ce* < 0.99, and 0.79 < Ce/Ce* < 0.99 for Logs 4, 1, and 6, respectively (Figure S2 in Supporting Information S1)) and the REE patterns acquire a small downward concavity specific of Middle REE (MREE) enrichment (0.62 < Pr/Gd < 0.97, 0.77 < Pr/Gd < 0.96,and 0.86 < Pr/Gd < 0.91 for Logs 4, 1, and 6, respectively) (Figure 8).

4.5. Sr and Nd Isotopes Fingerprinting

In order to better identify the provenance of clastic material and to distinguish possible changes in sources, Sr and Nd isotope analyses were performed on a few selected samples from Log 1. Results are presented in Table S2 in Supporting Information S1 and Figure 8. The variations of the $^{87}Sr/^{86}Sr$ ratio through depth again reflect the 3 different chemical compartments described above (Figure 8). In the upper compartment, $^{87}Sr/^{86}Sr$ ratios slightly decrease from 0.7505 close to the surface to 0.7398 at 1.7-m-deep. Below, the ratio decreases sharply to reach 0.7250 at 2.13 m, remaining around that value until increasing back to surface values (0.7459) below 4.5 m. By contrast, the $^{143}Nd/^{144}Nd$ ratios obtained on the same samples remain roughly constant through depth varying from 0.511639 to 0.511561.

4.6. Carbon and Oxygen Stable Isotopes

4.6.1. Carbon Isotopes in Waters

The $\delta^{13}C_{DOC}$ in water samples collected in November 2018 and July 2019 vary slightly depending on the sampling environment: river, alluvial plain, or groundwater in the central part of the island (Figures 2 and 9 and Table S3 in
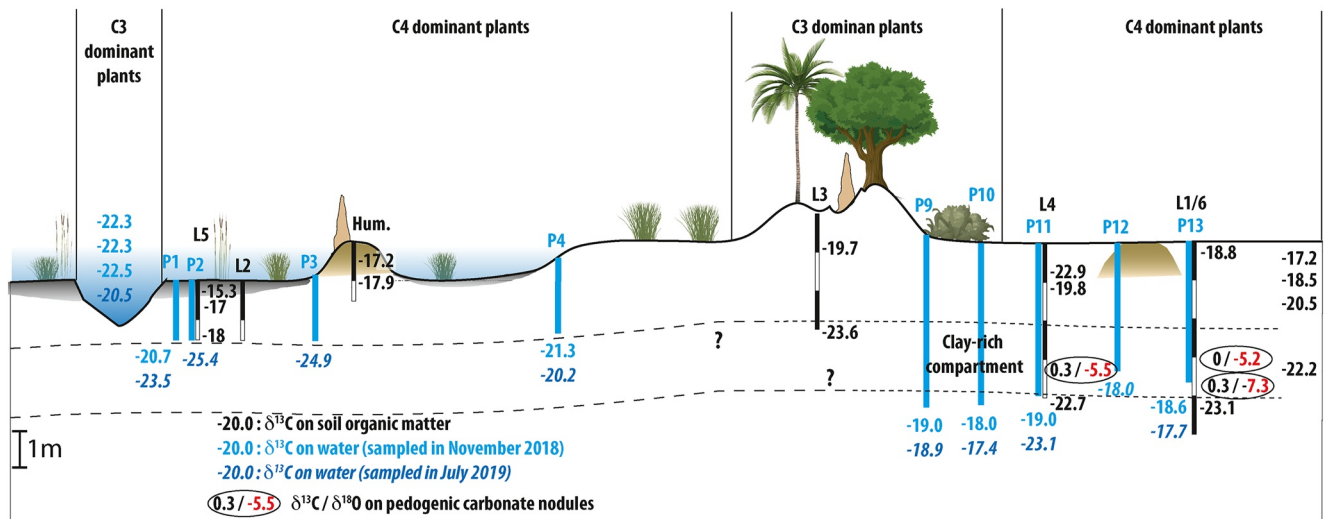
Figure 9. δ^{13}C isotopic rations of the organic matter within the sediments (black numbers) and waters (light blue and dark blue numbers depending on year of sampling) in and around Nxaraga Island as well as δ^{13}C and δ^{18}O isotopic ratios of the carbonate nodules in logs 1, 4, and 6 (values reported in a circle).

Supporting Information S1). All channels were either very low or dry. Waters sampled in the Boro River and its tributaries had δ^{13}C values of −22.3 ‰ to −22.5 ‰ in November 2018 and −20.5 ‰ in July 2019. In the alluvial plain, δ^{13}C$_{DOC}$ values ranged from −20.7 ‰ close to the river, to −21.3 ‰ in the middle of the floodplain. In 2019, the values were significantly different, ranging from −25.4 ‰ close to the river to −20.2 ‰ in the middle of the floodplain. Inside the island, the δ^{13}C values are significantly higher than in the floodplain or in the river, ranging from −19.0 ‰ to −18.0 ‰ in 2018 and −23.1 ‰ to −17.4 ‰ in 2019 (the value of −23.1 ‰ obtained for piezometer P11 (Figures 2 and 9) seems to be an outlier).

4.6.2. Carbon Isotopes in Sediments and Carbonate Nodules

The δ^{13}C values of the OM in sediments vary both geographically and with depth (Figure 9 and Table S3 in Supporting Information S1). In Log 5, near the Boro River, the values are relatively high, decreasing from −15.3 ‰ at the surface to −18.0 ‰ at 1.5 m depth. Two samples were acquired within the first meter from the surface in a small hummock supporting an active termite mound on the alluvial plain (marked Hum. on Figures 2 and 9). They provided values of −17.2 ‰ and −17.9 ‰ similar to those of Log 5. In the tree ring, samples from Log 3 showed a rapid decrease in δ^{13}C values from −19.7 ‰ at 1-m depth to −23.6 ‰ at 3-m depth. Note that the value of −19.7 ‰ is lower than all values obtained from the alluvial plain. In the bushes zone, the δ^{13}C results above 2 m depths were variable, with 2 values at −19.8 ‰ (consistent with that obtained in Log 3 at the same depth) and −22.9 ‰. At 4-m-depth, the value of −22.7 ‰ is consistent with the one obtained at 3 m in Log 3. In logs 1 and 6, the δ^{13}C results decrease systematically with depth, from −17.2 ‰ (Log 6) and −18.8 ‰ (Log 1) near the surface to −22.2 ‰ (Log 6) and −23.1 ‰ (Log 1) at depth below 2 m. Those values are consistent with those obtained in Log 4.

Finally, inorganic carbon and oxygen isotope ratios have been measured in pedogenic carbonate nodules from Log 4 and Log 1 (Figure 9 and Table S3 in Supporting Information S1). The δ^{13}C values are close to 0 ‰, whereas δ^{18}O values range from −5.2 ‰ to −7.3 ‰, possibly decreasing with increasing depth.

5. Discussion

5.1. Two Markedly Contrasted Geochemical Compartments

The sediment geochemical data allow distinguishing two different geochemical compartments. The first one is divided into two sub-compartments corresponding to the first 2–2.5 m of deposits, both in the alluvial plain and in the island, and below a depth of 4 m inside the island. The second compartment extends between 2 and 4 m in the island, associated to the variations in the water table (Dauteuil et al., 2021). The first compartment can be considered as the initial sandy material forming the Delta alluvial fan, while in the second one, the geochemical

pattern is strongly controlled by interactions between the sediment, the groundwater, and the OM. Furthermore, the lower compartment is systematically enriched in silt and clay compared to the upper one, with a sharp limit largely corresponding to the water table (Figure 4). The clay could result from on-site alteration of the sediment, mainly of feldspars. However, the amount of feldspar observed in all the samples is very low (Table 1 and Figure 5) and the increase in silt content, correlative to the increase in clay content, suggests a different depositional environment or sediment source than in the upper compartment. Finally, the overall mineralogical content of both compartments does not differ significantly (Table 1): the light minerals are essentially quartz with very few feldspars, and while the ZTR index content may vary, there is no direct link between the index value and the position of the sample in one or the other compartment. No REE-rich minerals such as monazite or xenotime were observed that could explain the differences in the REE patterns. Based on this result, we conclude that the variations in bulk chemical composition are not primarily driven by variations in the initial mineralogy of the sediment.

5.1.1. Geochemical Signature of the Upper Compartment

Major and trace element concentrations in surface sediments from the upper compartment (i.e., from 0 to about 2 m) are similar in the alluvial plain, the tree ring and the island (Figure 6 and Table S1). The high SiO_2 and very low CaO concentrations are consistent with the sediments formed by fine to medium grained, recycled Aeolian material containing mainly quartz (Garzanti et al., 2014; Haddon & McCarthy, 2005; Vainer et al., 2021). The low concentrations in K_2O and Na_2O as well as the absence of P_2O_5 advocate against the regular formation of a salt crust or efflorescent salt on the surface of Nxaraga Island, as described previously (Bauer-Gottwein et al., 2007). The hypothesis of such a deposit being washed from the surface by rainwater is further contradicted by the fact that some of the samples were collected during the exceptionally dry year 2019. The limited increase in Al_2O_3 and Fe_2O_3 concentrations with depth matches the increase in clay and possibly (Fe, Al) oxyhydroxides content, and the strong correlation between Al_2O_3, Rb and Cr (Figures 5d and 5e) indicates that these elements are largely associated with the clay fraction (Fendorf, 1995; Guo et al., 2014). However, the LOI is low (below 3%), indicating that the amounts of phyllosilicates and OM remain limited even in Logs 3 and 5 where OM is visible.

The $^{143}Nd/^{144}Nd$ isotopic ratio is constant through depth over the whole compartment and similar to the ratios observed in the surface sediment of the nearby islands (Humphries et al., 2020) or in the muddy fraction transported in the Boro channel (Garzanti et al., 2014) (Figure 8). This observation implies a relative initial bulk $^{143}Nd/^{144}Nd$ isotopic ratio homogeneity of all the grain-size fractions of the material. As mentioned above, this material forming most of the Okavango alluvial fan, is derived from the recycled Kalahari sand and from aeolian material both transported from the East and from the Makgadikgadi Pan to the South (Humphries et al., 2014, 2020; Vainer et al., 2021). Hereafter, we refer to this material as the "initial" sediment. The $^{87}Sr/^{86}Sr$ ratios obtained in the central part of the island fit within the upper range of values reported from the surface sediment of the surrounding islands (Humphries et al., 2020). However, those values vary between 0.7263 and 0.7608 for the bulk surface sediment, which contains variable proportions of the Kalahari coarse-grain sand and East Kalahari dust fractions mixed with fine-grained aeolian particles transported from the Makgadikgadi salty pans to the South (Humphries et al., 2020). These sediment sources that can be considered as end-members in terms of Sr isotopic signature are associated with strongly radiogenic Sr (ratios of 0.7451–0.7566) and less radiogenic Sr (ratios of 0.7226–0.7245) respectively. Low Sr radiogenic values are also found in the mud fraction from the Boro river, probably corresponding again to recycled wind-blown dust (Garzanti et al., 2014). Based on these observations, we consider that in the material forming the upper compartment in Nxaraga Island, Sr is mainly carried by the fluvial sandy fraction and the East Kalahari dust, with a limited influence from fine-grained material derived from the Makgadikgadi Pan. This is supported by the low clay and silt content measured in the upper compartment.

The REE patterns of Logs 1, 4, 5, and 6 within the first 0.5 m, all exhibit a HREE enrichment that tends to decrease with depth (Figure 7). By contrast, the REE patterns of Log 3 are close in shape with that of the mud fraction of the Boro sediments (Garzanti et al., 2014) (Figures 7 and 10). Close to the surface, no carbonate nodules were observed, and REE can be associated either with accessory minerals such as monazite, Fe-enriched clay (see Section 4.3) or OM since these are major REE carriers (Dia et al., 2000; Marsac et al., 2013; Pédrot et al., 2015). The petrographic data obtained in all the various sedimentary compartments indicate no major variations, both in the amount and type of heavy minerals. No monazite was observed. This suggests that heavy minerals do not drive the REE content. The lowest ΣREE and the highest HREE enrichments are observed in Logs 1 and 4 where OM amount visually appears to be minimum (Table S1). Moreover, several authors demonstrated
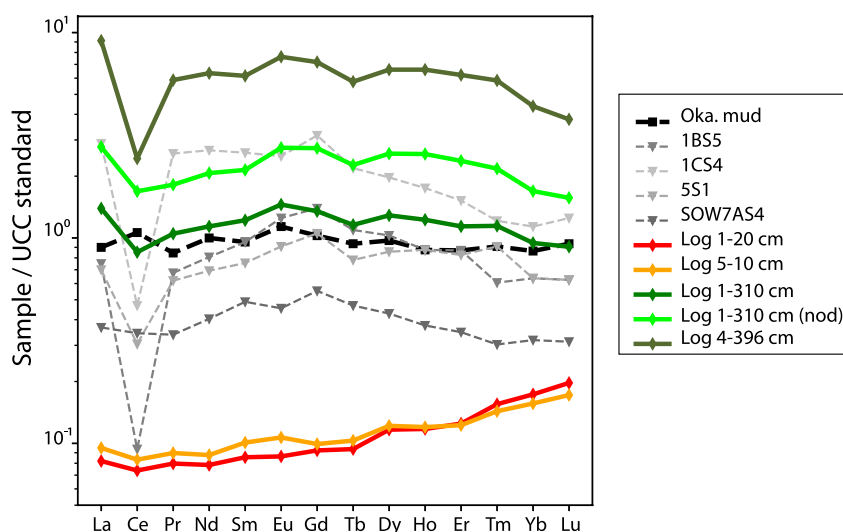
Figure 10. Comparison between rare earth elements patterns displayed by key samples from Nxaraga area (logs 1, 4, and 5) and some data from the literature. Sample Oka. Mud is the mud fraction of the Boro channel (Garzanti et al., 2014); samples 1BS5,1CS4, and 5S1 are calcretes from the southern Makgadikgadi Basin (Kampunzu et al., 2007); and sample SOW7AS4 is a carbonate duricrust from the eastern Makgadikgadi Basin (Ringrose et al., 2009).

that REE patterns of REE bound to OM exhibit a MREE downward concavity not observed for these uppermost REE patterns (e.g., Marsac et al., 2010; Pourret et al., 2007) (Figure 7). By contrast, Coppin et al. (2002) demonstrated that the REE pattern obtained for clays (kaolinite and smectite) exhibited a marked HREE enrichment for high ionic strength environments. We can therefore conclude that REE patterns obtained in the uppermost layer of the Logs 1, and 4 correspond to REE bound to clays that are more specifically sourced from the Kalahari aeolian dust (especially HREE-enriched smectite) trapped in the central parts of the islands (Humphries et al., 2020). In Logs 5 and 6, both the HREE enrichment and the ΣREE are slightly lower (Figure 7 and Table S1). This may be attributed to an increase of less HREE-enriched alluvial clay fraction (Garzanti et al., 2014; Krah et al., 2004).

Although in Log 3 ΣREE was the lowest at the surface, the REE patterns are similar to that of the Boro muddy fraction (Figures 7 and 10). This is consistent with the location of the Log 3; namely on the topographic ridge limiting the floodplain and the barren zone, below the tree ring. The trees trap the near-*in situ* fine-grained particles produced on the floodplain during the dry season (Krah et al., 2004) as well as the exogenous East Kalahari wind-borne supply (Humphries et al., 2020). Indeed, from all drill holes, Log 3 displays the highest amount of clay within the first meter-depth. This addition of dust forms a fine-grained material with a composition close to that of the initial material of the alluvial fan. The slight enrichment in HREE may correspond to a higher proportion of Kalahari dust as compared to alluvium-derived dust.

5.1.2. The Water Table Compartment

Due to the long-term (millions of years) semi-arid climate, duricrusts including calcretes, silcretes and mixed sil-calcretes, are exposed widely in Southern Africa, covering large areas of the Kalahari Desert (Dill et al., 2014; Kampunzu et al., 2007; Nash & McLaren, 2003; Ringrose et al., 2005, 2009; Thomas et al., 2003). Both sedimentological and geochemical data reported in this study demonstrate that the sedimentary compartment enclosed within the water table fluctuation zone in Nxaraga Island (from about 2 to 4 m) is affected by incipient calcretisation.

In Logs 1, 4, and 6, the coeval increase in the concentration of CaO and most major and trace elements directly correlate with the occurrence of carbonate nodules. However, the sediments also display a sharp increase in clay (up to ~30% in Log 4) in regards to SiO_2 contents (Figure 6). Calcification and chemical enrichment processes reach a maximum at around 3.5–4 m from the surface before decreasing back to near-surface concentrations around 4.5 m depth. Carbonate precipitation in the water table fluctuation zone is favored by the high pH (>8) of the groundwater (Dauteuil et al., 2021; Ramberg & Wolski, 2008; Wolski et al., 2005). The REE patterns in the sediments are controlled by carbonate nodules (Figures 7 and 10). Finally, the sediment REE pattern mirrors

the water REE pattern reported by Dauteuil et al. (2021), suggesting that water and sediment are at equilibrium: the groundwater REE pattern exhibits both a strong HREE enrichment and a positive Ce anomaly. Regarding Ce anomaly, Pourret et al. (2007) demonstrated that in conditions of organic-rich water and pH = 9 similar to that reported by Dauteuil et al. (2021) (dissolved organic carbon concentration up to 1,200 mgL^{-1} and pH ≈ 9), high concentrations of carbonates promote the oxidation of Ce(III) as Ce(IV). Cerium(IV) as a tetravalent ion is then preferentially adsorbed by colloidal OM, which results in the development of a positive Ce anomaly in the water REE patterns.

Although the Nd concentrations increase about 10-fold compared to the surface sediments in Log 1 (Table S1), the ^{143}Nd/^{144}Nd ratios remain comparable to those observed in the upper compartment, suggesting a common Nd source (Figure 8 and Table S1). However, the ^{87}Sr/^{86}Sr ratios decrease sharply and significantly. As Sr isotopes are not fractionated by hydrological processes, evaporation, or biological activity (Capo et al., 1998; Graustein, 1989; Peterman et al., 1992), a new source of material must have been incorporated to the sediment, imprinting its Sr radiogenic signature. The aeolian dust originating from the Makgadikgadi Pan has a ^{143}Nd/^{144}Nd of 0.511780–0.511854 very close to that observed in the Nxaraga sediments (0.511561–0.511639) and a ^{87}Sr/^{86}Sr ratio of 0.7223–0.7245 (Humphries et al., 2020) close to the value of 0.7249–0.7250 in the water-table compartment. Furthermore, while the Sr concentration observed in the Okavango surface sediment is of the order of 5–30 ppm, it reaches a mean concentration of 157 ppm in the Makgadikgadi sediments (Humphries et al., 2020). We thus consider that the Sr isotope ratio decrease observed in the water table compartment of Nxaraga Island is associated with an exceptionally high proportion of Sr-rich dust derived from the Makgadikgadi Pan, and especially from the reworking of the abundant calcrete layers (and thus possibly to a drier-climate period) (Garzanti et al., 2022). While age constrains on the sediments are lacking, this high dust influx may correspond in time to the last very arid period between 15 and 9 ka (Telfer & Thomas, 2007).

5.2. Are Both Compartments Geochemically and Hydrologically Connected?

The surface compartment described above extends horizontally over the alluvial plain, the tree-covered ridge and the barren zone (Figure 11). The limited geochemical differences observed laterally are related to the amount of (a) dust produced in situ or imported from the Kalahari desert and Makgadikgadi pan, and spread all over the islands as well as (b) OM and associated oxides.

The geometry and extension of the water table compartment are more difficult to constrain. All the existing hydrogeological models suggest a water table continuity between the channel—floodplain system and the central part of the islands. These models imply a deepening of the water table below the islands as the salinity increases, with a strong slope of the water table level and a high salinity gradient crossing the tree-ring (McCarthy, 2006; Milzow et al., 2009; Ramberg & Wolski, 2008; Wolski & Savenije, 2006). Water table variations are high in the floodplain (1–2 m) and low in the central part of the island (0.5 m) (Dauteuil et al., 2021; Wolski & Savenije, 2006). The lateral influence of annual flooding on the water table decreases away from the channels and rainfall recharge is limited and not systematic. The groundwater flow from the channel toward the island is controlled by the vegetation demand, evapotranspiration and evaporation (Wolski & Savenije, 2006).

Although they are extensively documented, those models are relying on water table measurements in piezometers that are 2- to 11-m-deep (Wolski & Savenije, 2006). Some of them (especially in the floodplain where the soil is rapidly saturated in water) do not penetrate deep enough to reach the potentially existing lower compartment. Based on REE patterns in waters, Dauteuil et al. (2021) demonstrated that the geochemical composition of the groundwater inside the island could not be simply obtained by chemical concentration through the evaporation of the surface water (evaporation does not fractionate REE elements). Furthermore, our data indicate that the REE patterns of both waters and sediments in the groundwater compartment are controlled by exchanges between water, carbonates and OM, and not by the evaporation process.

The lack of water exchange between the two compartments is also consistent with the δ^{13}C values of OM obtained in this study (Figure 9). The δ^{13}C values of the water from the channels and groundwater in the floodplain are similar, with a strong C3 plant fingerprint (Kohn, 2010; Strömberg, 2011). However, our values are higher than those obtained by Akoko et al. (2013), indicating that the C3 fingerprint might be even higher than what we observed. This low isotopic ratio reflects the mixed source of the water in the C3-plants-dominated rainforests of Angola as well as OM derived from C3-dominated ecosystems of the channels (Ramberg et al., 2006; Tsheboeng, 2018). The δ^{13}C values of soil OM in the floodplain are high, reflecting a strong fingerprint from C4
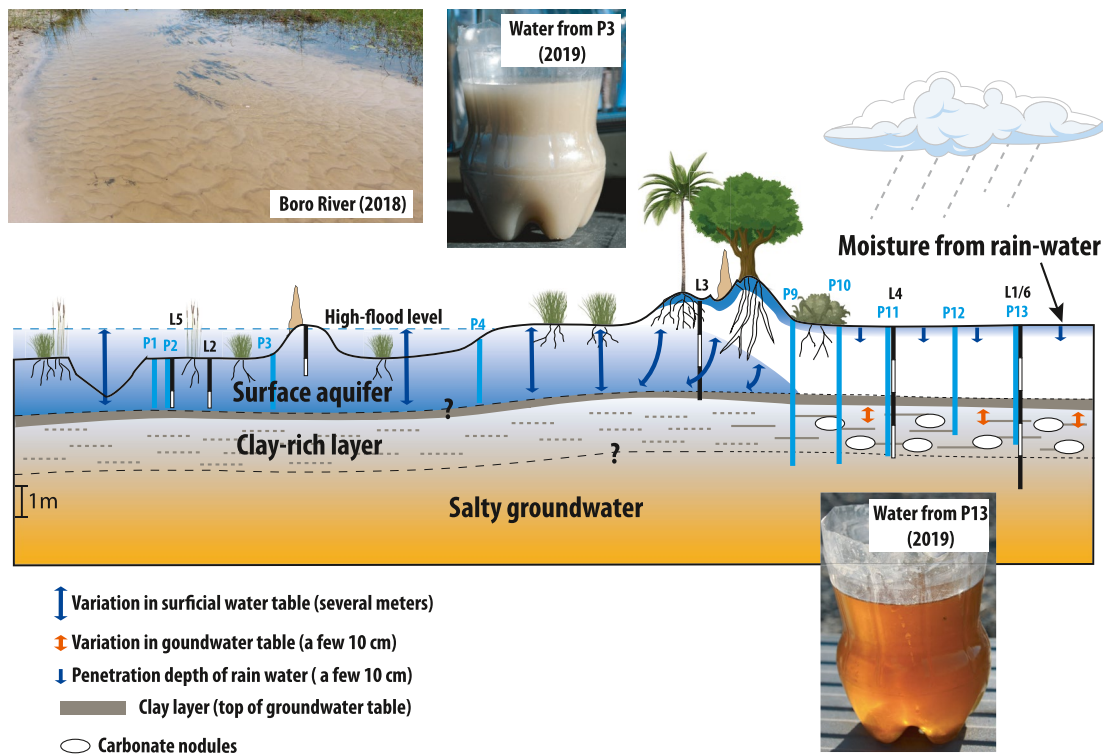
Figure 11. Proposed hydrological model involving two very different aquifers separated by a clay layer. The saline aquifer (water is orange suggesting the high mineral concentrations) is seal-capped by the clay layer, disconnecting it from the surface freshwater aquifer (as shown on the river picture, the water is very clear without suspended clay load) linked to the flood. While the vegetation on the floodplain and tree ring has access to freshwater, the vegetation inside the island only relies on rainwater during summer. The "white water" sample containing a high clay content was extracted from piezometer P3 during the anomalously dry period of July 2019. Clay from the clay layer at the bottom of the piezometer was put into suspension by the pumping operation. See text for detailed discussion.

grasses. This contrast between water and soil OM $\delta^{13}C$ values (Table S3 in Supporting Information S1) suggests that the groundwater in the floodplain records its river-originated signature.

The soil OM $\delta^{13}C$ values decrease significantly in the tree ring and bush zones due to the input of C3 plants (trees and some bushes). Finally, in the barren zone, the $\delta^{13}C$ values are variable between C3-type pool and C4-type pool. Note that the higher near-surface values (−17.2 ‰ and −18.5 ‰) were obtained in Log 6, in an area of the barren zone directly connected to the C4-dominated alluvial plain (Figure 9 and Table S3 in Supporting Information S1). However, below the groundwater level, $\delta^{13}C$ values are strongly depleted, implying a different OM than at the surface. In the bushes' zone and central part of the island, the $\delta^{13}C$ values of the groundwater are significantly higher than that of the floodplain water (except one value at −23.1 ‰ that we consider as an outlier) and again in strong disequilibrium with the local soil OM. Finally, the carbon and oxygen isotopic values of the carbonate nodules are consistent with Quaternary carbonates developing in a semi-arid, strongly C4-fingerprinted environment (Jolivet & Boulvais, 2021 and references therein), thus in equilibrium with the water rather than with the soil OM. Assuming no equilibration of carbon isotopic ratios between soil OM and water, recharge of the groundwater in the central part of the island from floodwater should result in a homogeneous $\delta^{13}C$ ratio between the two water compartments. Should partial equilibration occur between soil OM and water in the underground compartment, the low $\delta^{13}C$ ratio of the deep soil OM should further decrease the water isotopic composition and not increase it. This further supports the hypothesis of two different water sources and reservoirs as proposed by Dauteuil et al. (2021).

Based on those results, we propose a new version of the Dauteuil et al. (2021) hydrological model (Figure 11) composed of two non-connected aquifers. The clay-rich layer observed in all the drillings inside the island probably extends laterally to the floodplain. Indeed, during the very dry 2019 summer water collected at the very bottom of piezometer P3 at 1.6 m depth was exceptionally clay-rich, indicating that the sediment at the base of the piezometer is strongly enriched in clay compared to the surface deposits. In comparison, the water in the

Boro River that participates in the same aquifer is very clear (Figure 11). This clay-rich layer caps the saline groundwater aquifer isolating it from the surface, fresh-water aquifer. The groundwater level varies only by a few tens of centimeters (Dauteuil et al., 2021), allowing for the formation of an incipient carbonate paleosoil immediately below the clay-cap. The surface aquifer varies by several meters following the annual flood (Dauteuil et al., 2021 and references therein). Infiltration toward the inside of the island is facilitated but limited by the intense water-pumping of the vegetation in the tree-ring area (Milzow et al., 2009; Ramberg et al., 2006; Ramberg & Wolski, 2008). Inside the island, the vegetation has no access to freshwater except for rainwater during the summer. However, due to the high evaporation potential, this rainwater does not infiltrate deep, preventing water storage inside the island.

Though the incoming floodwater has low pH and conductivity (Dauteuil et al., 2021), Oromeng et al. (2021) estimated that it brings annually about 329,200 Mg/y of dissolved solutes in the Delta. From these, 21% are removed, flushed out of the system by the flood or rainwater, leaving 260,960 Mg/y of solute in the Delta (Letshele et al., 2023; Oromeng et al., 2021; Ramatapleng et al., 2021, 2023). However, the fate of these solutes remains to be understood. Based on the results presented above, the solutes that remain in the Delta do not participate to the brine stored below the islands. Could they be consumed by the annually growing vegetation? Furthermore, the solutes flushed from the Delta by the flood should end-up either in Lake Ngami (through the Kunyere river) or Lake Xau (through the Boteti river) (Figure 1) although these do not show major salt input (Meier et al., 2015).

6. Conclusions

The presented data set demonstrates the strong influence of aeolian dust from the Makgadikgadi Pan in controlling the soil and water geochemistry of the SW Okavango alluvial fan. The clay-rich layer observed between about 2 and 2.5 and 4 m deep in Nxaraga Island seems directly related to a massive input of this dust within deposits otherwise mainly composed of recycled aeolian sand. The limited variations in water table within that clay-rich compartment allow for strong geochemical enrichment and the development of an incipient calcrete layer at depth. The contrasted geochemistry of the sediment compartments as well as that of the associated waters question the previous hydro-geochemical models explaining the evolution of the Okavango islands. Indeed, the clay-rich layer represents a hydrological barrier disconnecting the groundwater aquifer from the surface, flood-controlled one. This disconnection is further supported by the fact that the geochemistry of both the sediment and the water in the groundwater aquifer cannot be explained by the usually accepted evaporation, evapotranspiration and flood-water recharge processes. Indeed, since 98% of the floodwater is lost through evapotranspiration, the fate of the precipitate produced by this mechanism remains to be understood. Finally, the lateral extent of the clay layer and its associated geochemical pattern may not be restricted to the central part of the islands as previously suggested. Due to the potentially high toxicity of the groundwater for the ecosystems, it is thus of primary importance to document the lateral extent and the hydro-geochemical behavior of this saline aquifer. This is especially urgent in the present-day context of climate change and increasing anthropic pressure.

Data Availability Statement

The geochemistry results obtained in this study (major and trace elements, isotopic ratios) and grain size analysis data used to assess the geochemical and sedimentological patterns of the sediments in Nxaraga Island and the surrounding floodplain are available at Open Science Framework (OSF) data repository Jolivet, M. (2023, March 30). Geochemistry Botswana. Retrieved from osf.io/6h4rf. All data can be access free. The repository has been created and will be made public upon acceptance of publication.

References

Akoko, E., Atekwana, E. A., Cruse, A. M., Molwalefhe, L., & Masamba, W. R. L. (2013). River-wetland interaction and carbon cycling in a semi-arid riverine system: The Okavango Delta, Botswana. *Biogeochemistry*, *114*(1), 359–380. https://doi.org/10.1007/s10533-012-9817-x

Akondi, R. N., Atekwana, E. A., & Molwalefhe, L. (2019). Origin and chemical and isotopic evolution of dissolved inorganic carbon (DIC) in groundwater of the Okavango Delta, Botswana. *Hydrological Sciences Journal*, *64*(1), 105–120. https://doi.org/10.1080/02626667.2018.1560447

Assine, M. L., & Soares, P. C. (2004). Quaternary of the Pantanal, west-central Brazil. *Quaternary International*, *114*(1), 23–34. https://doi.org/10.1016/s1040-6182(03)00039-9

Atekwana, E. A., Molwalefhe, L., Kgaodi, O., & Cruse, A. M. (2016). Effect of evapotranspiration on dissolved inorganic carbon and stable carbon isotopic evolution in rivers in semi-arid climates: The Okavango Delta in North West Botswana. *Journal of Hydrology: Regional Studies*, *7*, 1–13. https://doi.org/10.1016/j.ejrh.2016.05.003

Bauer, P., Gumbricht, T., & Kinzelbach, W. (2006). A regional coupled surface water/groundwater model of the Okavango Delta, Botswana. *Water Resources Research*, *42*(4), W04403. https://doi.org/10.1029/2005WR004234

Bauer, P., Thabeng, G., Stauffer, F., & Kinzelbach, W. (2004). Estimation of the evapotranspiration rate from diurnal groundwater level fluctuations in the Okavango Delta, Botswana. *Journal of Hydrology*, *288*(3), 344–355. https://doi.org/10.1016/j.jhydrol.2003.10.011

Bauer-Gottwein, P., Langer, T., Prommer, H., Wolski, P., & Kinzelbach, W. (2007). Okavango Delta Islands: Interaction between densi-ty-driven flow and geochemical reactions under evapo-concentration. *Journal of Hydrology*, *335*(3), 389–405. https://doi.org/10.1016/j.jhydrol.2006.12.010

Bufford, K. M., Atekwana, E. A., Abdelsalam, M. G., Shemang, E., Atekwana, E. A., Mickus, K., et al. (2012). Geometry and faults tectonic activity of the Okavango Rift Zone, Botswana: Evidence from magnetotelluric and electrical resistivity tomography imaging. *Journal of African Earth Sciences*, *65*, 61–71. https://doi.org/10.1016/j.jafrearsci.2012.01.004

Burrough, S. L., & Thomas, D. S. G. (2013). Central southern Africa at the time of the African humid period: A new analysis of Holocene palaeoenvironmental and palaeoclimate data. *Quaternary Science Reviews*, *80*, 29–46. https://doi.org/10.1016/j.quascirev.2013.08.001

Burrough, S. L., Thomas, D. S. G., & Bailey, R. M. (2009). Mega-Lake in the Kalahari: A late Pleistocene record of the Palaeolake Makgadikgadi system. *Quaternary Science Reviews*, *28*(15–16), 1392–1411. https://doi.org/10.1016/j.quascirev.2009.02.007

Campbell, G., Johnson, S., Bakaya, T., Kumar, H., & Nsatsi, J. (2006). Airborne geophysical mapping of aquifer water quality and structural controls in the Lower Okavango Delta, Botswana. *South African Journal of Geology*, *109*(4), 475–494. https://doi.org/10.2113/gssajg.109.4.475

Capo, R. C., Stewart, B. W., & Chadwick, O. A. (1998). Strontium isotopes as tracers of ecosystem processes: Theory and methods. *Geoderma*, *82*(1–3), 197–225. PII S0016-7061(97)00102-X. https://doi.org/10.1016/s0016-7061(97)00102-x

Coppin, F., Berger, G., Bauer, A., Castet, S., & Loubet, M. (2002). Scorption of lanthanides on smectite and kaolinite. *Chemical Geology*, *182*(1), 57–68. PII : S0009-2541(01)00283-2. https://doi.org/10.1016/s0009-2541(01)00283-2

Dangerfield, J. M., McCarthy, T. S., & Ellery, W. N. (1998). The mound-building termite *Macrotermes michaelseni* as an ecosystem engineer. *Journal of Tropical Ecology*, *14*(4), 507–520. https://doi.org/10.1017/s0266467498000364

Dauteuil, O., Jolivet, M., Dia, A., Murray-Hudson, M., Makati, K., Barrier, L., et al. (2021). Trace metal enrichments in water of the Okavango Delta (Botswana): Hydrological consequences. *Geochemistry, Geophysics, Geosystems*, *22*(5), e2021GC009856. https://doi.org/10.1029/2021GC009856

Davies, A. B., Levick, S. R., Asner, G. P., Robertson, M. P., van Rensburg, B. J., & Parr, C. L. (2014). Spatial variability and abiotic determinants of termite mounds throughout a savanna catchment. *Ecography*, *37*(9), 852–862. https://doi.org/10.1111/ecog.00532

Dia, A., GruauOlivié-Lauquet, G. G., Riou, C., Molénat, J., & Curmi, P. (2000). The distribution of rare Earth elements in shallow groundwaters: Assessing the role of source-rock composition, redox conditions and colloidal particles. *Geochimica et Cosmochimica Acta*, *64*(24), 4131–4151. https://doi.org/10.1016/s0016-7037(00)00494-4

Dill, H. G., Dohrmann, R., Kaufhold, S., & Techmer, A. (2014). Provenance analysis and thermo-dynamic studies of multi-type Holocene duricrusts (1700 BC) in the Sua Salt Pan, NE Botswana. *Journal of African Earth Sciences*, *96*, 79–98. https://doi.org/10.1016/j.jafrearsci.2014.03.014

Ellery, W. N., Ellery, K., Rogers, K. H., McCarthy, T. S., & Walker, B. H. (1993). Vegetation, hydrology and sedimentation processes as determinants of channel form and dynamics in the northeastern Okavango Delta, Botswana. *African Journal of Ecology*, *31*(1), 10–25. https://doi.org/10.1111/j.1365-2028.1993.tb00514.x

Ellery, W. N., & McCarthy, T. S. (1994). Principles of sustainable utilization of the Okavango Delta ecosystem, Botswana. *Biological Conservation*, *70*(2), 159–168. https://doi.org/10.1016/0006-3207(94)90284-4

Fairhead, J. D., & Girdler, R. W. (1969). How far does the rift system extend through Africa. *Nature*, *221*(5185), 1018–1020. https://doi.org/10.1038/2211018a0

Fendorf, S. E. (1995). Surface reactions of chromium in soils and waters. *Geoderma*, *67*(1–2), 55–71. SSDI 0016-7061(94)00062-X. https://doi.org/10.1016/0016-7061(94)00062-f

Garstang, M., Ellery, W. N., McCarthy, T. S., Scholes, M. C., Scholes, R. J., Swap, R. J., & Tyson, P. D. (1998). The contribution of aerosol- and water-borne nutrients to the functioning of the Okavango Delta ecosystem, Botswana. *South African Journal of Science*, *94*, 223–229.

Garzanti, E. (2019). Petrographic classification of sand and sandstone. *Earth-Science Reviews*, *192*, 545–563. https://doi.org/10.1016/j.earscirev.2018.12.014

Garzanti, E., Padoan, M., Setti, M., López-Galindo, A., & Villa, I. M. (2014). Provenance versus weathering control on the composition of tropical river mud (southern Africa). *Chemical Geology*, *366*, 61–74. https://doi.org/10.1016/j.chemgeo.2013.12.016

Garzanti, E., Pastore, G., Stone, A., Vainer, S., Vermeesch, P., & Resentini, A. (2022). Provenance of Kalahari Sand: Paleoweathering and recycling in a linked fluvial-Aeolian system. *Earth-Science Reviews*, *224*, 103867. https://doi.org/10.1016/j.earscirev.2021.103867

Gieske, A. (1997). Modelling outflow from the Jao/Boro system in the Okavango Delta, Botswana. *Journal of Hydrology*, *193*(1–4), 214–239. https://doi.org/10.1016/s0022-1694(96)03147-2

Graustein, W. C. (1989). [87]Sr/[86]Sr ratios measure the source and flow of strontium in terrestrial ecosystems. In P. W. Rundel, et al. (Eds.), *Stable isotopes in ecological research* (pp. 491–512). Springer-Verlag.

Grove, A. T. (1969). Landforms and climatic change in the Kalahari and Ngamiland. *The Geographical Journal*, *135*(2), 191–212. https://doi.org/10.2307/1796824

Gumbricht, T., & McCarthy, T. S. (2003). Spatial patterns of islands and salt crusts in the Okavango Delta, Botswana. *South African Geographical Journal*, *85*(2), 164–169. https://doi.org/10.1080/03736245.2003.9713797

Gumbricht, T., Wolski, P., Frostc, P., & McCarthya, T. S. (2004). Forecasting the spatial extent of the annual flood in the Okavango Delta, Botswana. *Journal of Hydrology*, *290*(3–4), 178–191. https://doi.org/10.1016/j.jhydrol.2003.11.010

Guo, Y., Li, B., Wen, X., Wang, F., Niu, D., Shi, Y., et al. (2014). Holocene climate variation determined from rubidium and strontium contents and ratios of sediments collected from the BadainJaran Desert, Inner Mongolia, China. *Chemie der Erde*, *74*(4), 571–576. https://doi.org/10.1016/j.chemer.2013.09.001

Haddon, I. G., & McCarthy, T. S. (2005). The Mesozoic—Cenozoic interior sag basins of central Africa: The late-cretaceous—Cenozoic Kalahari and Okavango basins. *Journal of African Earth Sciences*, *43*(1–3), 316–333. https://doi.org/10.1016/j.jafrearsci.2005.07.008

Hughes, D. A., Andersson, L., Wilk, J., & Savenije, H. H. G. (2006). Regional calibration of the pitman model for the Okavango River. *Journal of Hydrology*, *331*(1–2), 30–42. https://doi.org/10.1016/j.jhydrol.2006.04.047

Humphries, M. S., Benitez-Nelson, C. R., Bizimis, M., Ralph, T. J., Larkin, Z. T., & McCarthy, T. S. (2020). Dust provenance and its role as a potential fertilizing agent for the Okavango Delta, Botswana. *Earth Surface Processes and Landforms*, *45*(8), 1705–1716. https://doi.org/10.1002/esp.4840

Humphries, M. S., McCarthy, T. S., Cooper, G. R. J., Stewart, R. A., & Stewart, R. D. (2014). The role of airborne dust in the growth of tree islands in the Okavango Delta, Botswana. *Geomorphology*, *206*, 307–317. https://doi.org/10.1016/j.geomorph.2013.09.035

Huntsman-Mapila, P., Kampunzu, A. B., Vink, B., & Ringrose, S. (2005). Cryptic indicators of provenance from the geochemistry of the Okavango Delta sediments, Botswana. *Sedimentary Geology*, *174*(1–2), 123–148. https://doi.org/10.1016/j.sedgeo.2004.11.001

Huntsman-Mapila, P., Mapila, T., Letshwenyo, M., Wolski, P., & Hemond, C. (2006). Characterization of arsenic occurrence in the water and sediments of the Okavango Delta, NW Botswana. *Applied Geochemistry*, *21*(8), 1376–1391. https://doi.org/10.1016/j.apgeochem.2006.05.003

Huntsman-Mapila, P., Nsengimana, H., Torto, & N., & Diskin, S. (2011). Arsenic distribution and geochemistry in island groundwater of the Okavango delta in Botswana. In J. Jones (Ed.), *Sustaining groundwater resources. International year of planet Earth*. Springer. https://doi.org/10.1007/978-90-481-3426-7_4

Ingersoll, R. V., Bullard, T. F., Ford, R. L., Grimm, J. P., Pickle, J. D., & Sares, S. W. (1984). The effect of grain size on detrital modes: A test of the Gazzi-Dickinson point-counting method. *Journal of Sedimentary Petrology*, *54*, 103–116.

Jolivet, M., & Boulvais, P. (2021). Global significance of oxygen and carbon isotope compositions of pedogenic carbonates since the Cretaceous. *Geoscience Frontiers*, *12*(4), 101132. https://doi.org/10.1016/j.gsf.2020.12.012

Jolivet, M., Dauteuil, O., & Gaudaré, L. (2022). Blowing the rivers: Regional-scale control of the drainage network by wind in northern Kalahari (Africa). *Geomorphology*, *398*, 108039. https://doi.org/10.1016/j.geomorph.2021.108039

Kampunzu, A. B., Ringrose, S., Huntsman-Mapila, P., Harris, C., Vink, B. W., & Matheson, W. (2007). Origins and palaeo-environments of Kalahari duricrusts in the Moshaweng dry valley (Botswana) as detected by major and trace element composition. *Journal of African Earth Sciences*, *48*(2–3), 199–221. https://doi.org/10.1016/j.jafrearsci.2006.10.007

Kenabatho, P. K., Parida, B. P., & Moalafhi, D. B. (2012). The value of large-scale climate variables in climate change assessment: The case of Botswana's rainfall. *Physics and Chemistry of the Earth, Parts A/B/C*, *50–52*, 64–71. https://doi.org/10.1016/j.pce.2012.08.006

Kinabo, B. D., Atekwana, E. A., Hogan, J. P., Modisi, M. P., Wheaton, D. D., & Kampunzu, A. B. (2007). Early structural development of the Okavango rift zone, NW Botswana. *Journal of African Earth Sciences*, *48*(2–3), 125–136. https://doi.org/10.1016/j.jafrearsci.2007.02.005

Kohn, M. J. (2010). Carbon isotope compositions of terrestrial C3 plants as indicators of (paleo)ecology and (paleo)climate. *Proceedings of the National Academy of Sciences of the United States of America*, *107*(46), 19691–19695. https://doi.org/10.1073/pnas.1004933107

Krah, M., McCarthy, T. S., Annegarn, H., & Ramberg, L. (2004). Airborne and dust deposition in the Okavango Delta, Botswana and its impact on landforms. *Earth Surface Processes and Landforms*, *29*(5), 565–577. https://doi.org/10.1002/esp.1051

Letshele, K. P., Atekwana, E. A., Molwalefhe, L., Ramatlapeng, G. J., & Masamba, W. R. L. (2023). Stable hydrogen and oxygen isotopes reveal aperiodic non-river evaporative solute enrichment in the solute cycling of rivers in arid watersheds. *Science of the Total Environment*, *856*, 159113. https://doi.org/10.1016/j.scitotenv.2022.159113

Livingstone, D. (1857). *Missionary travels and researches in South Africa*. Salzwasser Verlag. (reprint of original). ISBN/EAN: 9783861951803.

Marsac, R., Davranche, M., Gruau, G., & Dia, A. (2010). Metal loading effect on rare Earth element binding to humic acid: Experimental and modelling evidence. *Geochimica et Cosmochimica Acta*, *74*(6), 1749–1761. https://doi.org/10.1016/j.gca.2009.12.006

Marsac, R., Davranche, M., Gruau, G., Dia, A., Pédrot, M., Le Coz-Bouhnik, M., & Briant, N. (2013). Effects of Fe competition on REE binding to humic acid: Origin of REE pattern variability in organic waters. *Chemical Geology*, *342*, 119–127. https://doi.org/10.1016/j.chemgeo.2013.01.020

McCarthy, T. S. (2006). Groundwater in the wetlands of the Okavango Delta, Botswana, and its contribution to the structure and function of the ecosystem. *Journal of Hydrology*, *320*(3), 264–282. https://doi.org/10.1016/j.jhydrol.2005.07.045

McCarthy, T. S. (2013). The Okavango Delta and its place in the geomorphological evolution of Southern Africa. *South African Journal of Geology*, *116*(1), 1–54. https://doi.org/10.2113/gssajg.116.1.1

McCarthy, T. S., Barry, M., Bloem, A., Ellery, W. N., Heister, H., Merry, C. L., et al. (1997). The gradient of the Okavango fan, Botswana, and its sedimentological and tectonic implications. *Journal of African Earth Sciences*, *24*(1–2), 65–78. https://doi.org/10.1016/s0899-5362(97)00027-4

McCarthy, T. S., & Ellery, W. N. (1994). The effect of vegetation on soil and ground water chemistry and hydrology of islands in the seasonal swamps of the Okavango Fan, Botswana. *Journal of Hydrology*, *154*(1–4), 169–193. https://doi.org/10.1016/0022-1694(94)90216-x

McCarthy, T. S., Ellery, W. N., & Dangerfield, J. M. (1998). The role of biota in the initiation and growth of islands on the flood-plain of the Okavango alluvial fan, Botswana. *Earth Surface Processes and Landforms*, *23*(4), 291–316. https://doi.org/10.1002/(SICI)1096-9837(199804)23:4<291::AID-ESP844>3.0.CO;2-A

McCarthy, T. S., Ellery, W. N., & Ellery, K. (1993). Vegetation-induced, subsurface precipitation of carbonate as an aggradational process in the permanent swamps of the Okavango (Delta) fan, Botswana. *Chemical Geology*, *107*(1–2), 111–131. https://doi.org/10.1016/0009-2541(93)90105-r

McCarthy, T. S., Ellery, W. N., Rogers, K. H., Cairncross, B., & Ellery, K. (1986). The roles of sedimentation and plant growth in changing flow patterns in the Okavango Delta, Botswana. *South African Journal of Science*, *82*, 579–584.

McCarthy, T. S., Ellery, W. N., & Stanistreed, I. G. (1992). Avulsion mechanisms on the Okavango fan, Botswana: The control of a fluvial system by vegetation. *Sedimentology*, *39*(5), 779–795. https://doi.org/10.1111/j.1365-3091.1992.tb02153.x

McCarthy, T. S., McIver, J. R., & Verhagen, B. T. (1991). Groundwater evolution, chemical sedimentation and carbonate brine formation on an island in the Okavango Delta swamp, Botswana. *Applied Geochemistry*, *6*, 577–595. https://doi.org/10.1016/0883-2927(91)90071-v

McCarthy, T. S., Stanistreet, I. G., & Cairncross, B. (1991). The sedimentary dynamics of active fluvial channels on the Okavango fan, Botswana. *Sedimentology*, *38*(3), 471–487. https://doi.org/10.1111/j.1365-3091.1991.tb00362.x

Meier, S. D., Atekwana, E. A., Molwalefhe, L., & Atekwana, E. A. (2015). Processes that control water chemistry and stable isotopic composition during the refilling of Lake Ngami in semiarid northwest Botswana. *Journal of Hydrology*, *527*, 420–432. https://doi.org/10.1016/j.jhydrol.2015.04.050

Mendelsohn, J., & el Obeid, S. (2004). *The Okavango River*. Struik Publishers.

Milzow, C., Kgotlhang, L., Bauer-Gottwein, P., Meier, P., & Kinzelbach, W. (2009). Regional review: The hydrology of the Okavango Delta, Botswana—Processes, data and modelling. *Hydrogeology Journal*, *17*(6), 1297–1328. https://doi.org/10.1007/s10040-009-0436-0

Ministry of Mineral, Energy and Water Affairs. (1997). Maun groundwater development project phase 1: Exploration and resource assessment, final report (p. 53).

Mladenov, N., Huntsman-Mapila, P., Wolski, P., Masamba, W. R. L., & McKnight, D. M. (2008). Dissolved organic matter accumulation, reactivity, and redox state in ground water of a recharge wetland. *Wetlands*, *28*(3), 747–759. https://doi.org/10.1672/07-140.1

Mladenov, N., McKnight, D. M., Wolski, P., & Ramberg, L. (2005). Effects of annual flooding on dissolved organic carbon dynamics within a pristine wetland, the Okavango Delta, Botswana. *Wetlands*, *25*(3), 622–638. https://doi.org/10.1672/0277-5212(2005)025[0622:eoafod]2.0.co;2

Modisi, M., Atekwana, E., Kampunzu, A., & Ngwisanyi, T. (2000). Rift kinematics during the incipient stages of continental extension: Evidence from the nascent Okavango Rift basin, northwest Botswana. *Geology*, *28*(10), 939–942. https://doi.org/10.1130/0091-7613(2000)28<939:rkdtis>2.0.co;2

Moore, A. E., Cotterill, F. P. D., Eckardt, F. D., & Eckardt, F. D. (2012). The evolution and ages of Makgadikgadi palaeo-lakes: Consilient evidence from Kalahari drainage evolution south-central Africa. *South African Journal of Geology*, *115*(3), 385–413. https://doi.org/10.2113/gssajg.115.3.385

Mosley Bufford, K., Atekwana, E. A., Abdelsalam, M. G., Shemang, E., Atekwana, E. A., Mickus, K., et al. (2012). Geometry and faults tectonic activity of the Okavango Rift Zone, Botswana: Evidence from magnetotelluric and electrical resistivity tomography imaging. *Journal of African Earth Sciences*, *65*, 61–71. https://doi.org/10.1016/j.jafrearsci.2012.01.004

Muvengwi, J., Mbiba, M., Ndagurwa, H. G. T., & Kabvuratsiye, N. (2016). Pulsing hydrology and topography determine the structure and spatial distribution of *Cubitermes* mounds in a savanna ecosystem. *Catena*, *145*, 99–106. https://doi.org/10.1016/j.catena.2016.05.009

Nash, D. J., & McLaren, S. (2003). Kalahari valley calcretes: Their nature, origins, and environmental significance. *Quaternary International*, *111*(1), 3–22. https://doi.org/10.1016/S1040-6182(03)00011-9

Oromeng, K. V., Atekwana, E. A., Molwalefhe, L., & Ramatlapeng, G. J. (2021). Time-series variability of solute transport and processes in rivers in semi-arid endorheic basins: The Okavango Delta, Botswana. *Science of the Total Environment*, *759*, 143574. https://doi.org/10.1016/j.scitotenv.2020.143574

Pastier, A.-M., Dauteuil, O., Murray-Hudson, M., Moreau, F., Walpersdorf, A., & Makati, K. (2017). Is the Okavango Delta the terminus of the East African Rift System? Towards a new geodynamic model: Geodetic study and geophysical review. *Tectonophysics*, *712–713*, 469–481. https://doi.org/10.1016/j.tecto.2017.05.035

Pédrot, M., Dia, A., Davranche, M., & Gruau, G. (2015). Upper soil horizons control the rare Earth element patterns in shallow groundwater. *Geoderma*, *239–240*, 84–96. https://doi.org/10.1016/j.geoderma.2014.09.023

Peterman, Z. E., Stuckless, J. S., Mahan, S. A., Marshall, B. D., Gutentag, E. D., & Downey, J. S. (1992). Strontium isotope characterization of the Ash Meadows ground-water system, southern Nevada, USA. In Y. K. Karaka & A. S. Maest (Eds.), *Water-rock interaction: Proceedings of the 7th international symposium on water-rock interaction* (pp. 825–829). July 13–18, 1992.

Podgorski, J. E., Green, A. G., Kgotlhang, L., Kinzelbach, W. K. H., Kalscheuer, T., Auken, E., & Ngwisanyi, T. (2013). Paleo-megalake and paleo-megafan in southern Africa. *Geology*, *41*(11), 1155–1158. https://doi.org/10.1130/g34735.1

Pourret, O., Davranche, M., Gruau, G., & Dia, A. (2007). Competition between humic acid and carbonates for rare Earth elements complexation. *Journal of Colloid and Interface Science*, *305*(1), 25–31. https://doi.org/10.1016/j.jcis.2006.09.020

Ramatlapeng, G. J., Atekwana, E. A., & Molwalefhe, L. (2023). Spatial and temporal controls on the solute behavior of rivers in arid watersheds: The Okavango River, NW Botswana. *Journal of Hydrology*, *618*, 129141. https://doi.org/10.1016/j.jhydrol.2023.129141

Ramatlapeng, G. J., Atekwana, E. A., Molwalefhe, L., & Oromeng, K. V. (2021). Intermittent hydrologic perturbations control solute cycling and export in the Okavango Delta. *Journal of Hydrology*, *594*, 125968. https://doi.org/10.1016/j.jhydrol.2021.125968

Ramberg, L., & Wolski, P. (2008). Growing islands and sinking solutes: Processes maintaining the endorheic Okavango Delta as a freshwa-ter system. *Plant Ecology*, *196*(2), 215–231. https://doi.org/10.1007/s11258-007-9346-1

Ramberg, L., Wolski, P., & Krah, M. (2006). Water balance and infiltration in a seasonal floodplain in the Okavango Delta, Botswana. *Wetlands*, *26*(3), 677–690. https://doi.org/10.1672/0277-5212(2006)26[677:wbaiia]2.0.co;2

Ringrose, S. (2022). Landscape evolution of the Lake Ngami and Mababe depressions within the Okavango Rift Zone, North-Central Botswana. In F. D. Eckardt (Ed.), *Landscapes and landforms of Botswana* (pp. 57–75). Springer Nature Switzerland. https://doi.org/10.1007/978-3-030-86102-5

Ringrose, S., Harris, C., Huntsman-Mapila, P., Vink, B. W., Diskins, S., Vanderpost, C., & Matheson, W. (2009). Origins of strandlineduricrust around the Makgadikgadi Pans (Botswana Kalahari) as deduced from their chemical and isotope composition. *Sedimentary Geology*, *219*(1–4), 262–279. https://doi.org/10.1016/Jsedgeo.2009.05.021

Ringrose, S., Huntsman-Mapila, P., Basira Kampunzu, A., Downey, W. C., Coetzee, S., Vink, B., et al. (2005). Sedimentological and geochemical evidence for palaeo-environmental change in the Makgadikgadi subbasin, in relation to the MOZ rift depression, Btoswana. *Palaeogeography, Palaeoclimatology, Palaeoecology*, *217*(3–4), 265–287. https://doi.org/10.1016/j.palaeo.2004.11.024

Ringrose, S., Huntsman-Mapila, P., Downey, W., Coetzee, S., Fey, M., Vanderpost, C., et al. (2008). Diagenesis in Okavango fan and adjacent dune deposits with implications for the record of palaeo-environmental change in Makgadikgadi—Okavango—Zambezi basin, northern Botswana. *Geomorphology*, *101*(4), 544–557. https://doi.org/10.1016/j.geomorph.2008.02.008

Schuurman, G. (2006). Foraging and distribution patterns in a termite assemblage dominated by fungus-growing species in semi-arid northern Botswana. *Journal of Tropical Ecology*, *22*(03), 277–287. https://doi.org/10.1017/s0266467405003044

Schuurman, G., & Dangerfield, J. M. (1997). Dispersion and abundance of *Macrotermes michaelseni* colonies: A limited rôle for intraspecific competition. *Journal of Tropical Ecology*, *13*(1), 39–49. https://doi.org/10.1017/s0266467400010233

Stanistreet, I. G., Cairncross, B., & McCarthy, T. S. (1993). Low sinuosity and meandering Bedload rivers of the Okavango fan: Channel confinement by vegetated levées without fine sediment. *Sedimentary Geology*, *85*(1–4), 135–156. https://doi.org/10.1016/0037-0738(93)90079-k

Strömberg, C. A. E. (2011). Evolution of grasses and grassland ecosystems. *Annual Review of Earth and Planetary Sciences*, *39*(1), 517–544. https://doi.org/10.1146/annurev-earth-040809-152402

Taylor, S. R., & McLennan, S. M. (1985). *The continental crust: Its composition and evolution* (p. 312). Blackwell. https://www.osti.gov/biblio/6582885

Telfer, M. W., & Thomas, D. S. G. (2007). Late quaternary linear dune accumulation and chronostratigraphy of the southwestern Kalahari: Implications for Aeolian palaeoclimatic reconstructions and predictions of future dynamics. *Quaternary Science Reviews*, *26*(19–21), 2617–2630. https://doi.org/10.1016/j.quascirev.2007.07.006

Thomas, D. S. G., Brook, G., Shaw, P., Bateman, M., Haberyan, K., Appleton, C., et al. (2003). Late Pleistocene wetting and drying in the NW Kalahari: An integrated study from the Tsodili hills, Botswana. *Quaternary International*, *104*(1), 53–67. PII: S1040-6182(02)00135-0. https://doi.org/10.1016/s1040-6182(02)00135-0

Thomas, D. S. G., & Burrough, S. L. (2012). Interpreting geoproxies of late Quaternary climate change in African drylands: Implications for understanding environmental change and early human behaviour. *Quaternary International*, *253*, 5–17. https://doi.org/10.1016/j.quaint.2010.11.001

Tooth, S., McCarthy, T. S., Duller, G. A. T., Assine, M. L., Wolski, P., & Coetzee, G. (2021). Significantly enhanced mid Holocene fluvial activity in a globally important, arid-zone wetland: The Okavango Delta, Botswana. *Earth Surface Processes and Landforms*, *47*(3), 854–871. https://doi.org/10.1002/esp.5289

Tsheboeng, G. (2018). Spatial variation of the influence of distance from surface water on riparian plant communities in the Okavango Delta, Botswana. *Ecological Processes*, *7*(32), 32. https://doi.org/10.1186/s13717-018-0140-x

Tsheboeng, G., Murray-Hudson, M., & Kashe, K. (2017). Response of riparian plant communities to distance from surface water in the Okavango Delta, Botswana. *African Journal of Ecology*, *55*(4), 401–410. https://doi.org/10.1111/aje.12364

Vainer, S., Matmon, A., Erel, Y., Hidy, A. J., Crouvi, O., De Wit, M., et al. (2021). Landscape responses to intraplate deformation in the Kalahari constrained by sediment provenance and chronology in the Okavango Basin. *Basin Research*, *33*(2), 1170–1193. https://doi.org/10.1111/bre.12509

Vickery, K., & Eckardt, F. (2021). A closer look at mineral aerosol emmissions from the Makgadikgadi Pans, Botswana, using automated SEM-EDS (QEMSCAN®). *South African Geographical Journal*, *103*(1), 7–21. https://doi.org/10.1080/03736245.2020.1824805

Whitesides, C. J., & Butler, D. R. (2020). Biogeomorphology and zoogeomorphology. https://doi.org/10.1093/OBO/9780199874002-0061

Wilk, J., Kniveton, D., Andersson, L., Layberry, R., Todd, M. C., Hughes, D., et al. (2006). Estimating rainfall and water balance over the Okavango Riber Basin for hydrological applications. *Journal of Hydrology*, *331*(1–2), 18–29. https://doi.org/10.1016/j.jhydrol.2006.04.049

Wilson, B. H. (1973). Some natural and man-made changes in the channels of the Okavango Delta. *Botswana Notes and Records*, *5*, 132–153.

Wilson, B. H., & Dinçer, T. (1976). An introduction to the hydrology and hydrography of the Okavango Delta. In *Symposium on the Okavango delta* (pp. 33–48). Botswana Society.

Wolski, P., Murray-Hudson, M., Fernkvist, P., Lidén, A., Huntsman-Mapila, P., & Ramberg, L. (2005). Islands in the Okavango Delta as sinks of water-borne nutrients. *Botswana Notes and Records*, *37*, 253–263.

Wolski, P., & Savenije, H. H. G. (2006). Dynamics of floodplain-island groundwater flow in the Okavango Delta, Botswana. *Journal of Hydrology*, *320*(3–4), 283–301. https://doi.org/10.1016/j.jhydrol.2005.07.027

Wolski, P., Savenije, H. H. G., Murray-Hudson, M., & Gumbricht, T. (2006). Modelling of the flooding in the Okavango Delta, Botswana, using a hybrid reservoir-GIS model. *Journal of Hydrology*, *331*(1–2), 58–72. https://doi.org/10.1016/j.jhydrol.2006.04.040

Wolski, P., Stone, D., Tadross, M., Wehner, M., & Hewitson, B. (2014). Attribution of floods in the Okavango basin, southern Africa. *Journal of Hydrology*, *511*, 350–358. https://doi.org/10.1016/j.jhydrol.2014.01.055

Wolski, P., Todd, M. C., Murray-Hudson, M. A., & Tadross, M. (2012). Multi-decadal oscillations in the hydro-climate of the Okavango River system during the past and under a changing climate. *Journal of Hydrology*, *475*, 294–305. https://doi.org/10.1016/j.jhydrol.2012.10.018

Yapiyev, V., Sagintayev, Z., Inglezakis, V. J., Samarkhanov, K., & Verhoef, A. (2017). Essentials of endorheic and lakes: A review in the context of current and future water resource management and mitigation activities in central Asia. *Water*, *9*(10), 798. https://doi.org/10.3390/w9100798